

TOI-431/HIP 26013: a super-Earth and a sub-Neptune transiting a bright, early K dwarf, with a third RV planet

Ares Osborn, David J. Armstrong, Bryson Cale, Rafael Brahm, Robert A. Wittenmyer, Fei Dai, Ian J. M. Crossfield, Edward M. Bryant, Vardan Adibekyan, Ryan Cloutier, et al.

▶ **To cite this version:**

Ares Osborn, David J. Armstrong, Bryson Cale, Rafael Brahm, Robert A. Wittenmyer, et al.. TOI-431/HIP 26013: a super-Earth and a sub-Neptune transiting a bright, early K dwarf, with a third RV planet. Monthly Notices of the Royal Astronomical Society: Letters, 2021, 507 (2), pp.2782-2803. 10.1093/mnras/stab2313 . hal-03577486

HAL Id: hal-03577486
https://amu.hal.science/hal-03577486

Submitted on 16 Aug 2022

HAL is a multi-disciplinary open access archive for the deposit and dissemination of scientific research documents, whether they are published or not. The documents may come from teaching and research institutions in France or abroad, or from public or private research centers.

L'archive ouverte pluridisciplinaire **HAL**, est destinée au dépôt et à la diffusion de documents scientifiques de niveau recherche, publiés ou non, émanant des établissements d'enseignement et de recherche français ou étrangers, des laboratoires publics ou privés.



Distributed under a Creative Commons Attribution 4.0 International License

Monthly Notices of the ROYAL ASTRONOMICAL SOCIETY

MNRAS **507,** 2782–2803 (2021) https://doi.org/10.1093/mnras/stab2313
Advance Access publication 2021 August 11

TOI-431/HIP 26013: a super-Earth and a sub-Neptune transiting a bright, early K dwarf, with a third RV planet

Ares Osborn,[1,2★] David J. Armstrong,[1,2] Bryson Cale,[3] Rafael Brahm,[4,5] Robert A. Wittenmyer,[6] Fei Dai,[7] Ian J. M. Crossfield,[8] Edward M. Bryant,[1,2] Vardan Adibekyan,[9,10] Ryan Cloutier,[11,12] Karen A. Collins,[11] E. Delgado Mena,[9] Malcolm Fridlund,[13,14] Coel Hellier,[15] Steve B. Howell,[16] George W. King,[1,2] Jorge Lillo-Box,[17] Jon Otegi,[18,19] S. Sousa,[9,10] Keivan G. Stassun,[20] Elisabeth C. Matthews,[18,21] Carl Ziegler,[22] George Ricker,[21] Roland Vanderspek,[21] David W. Latham,[11] S. Seager,[21,23,24] Joshua N. Winn,[25] Jon M. Jenkins,[16] Jack S. Acton,[26] Brett C. Addison,[6] David R. Anderson,[1,2] Sarah Ballard,[27] David Barrado,[17] Susana C. C. Barros,[9,10] Natalie Batalha,[42] Daniel Bayliss,[1,2] Thomas Barclay,[28,29] Björn Benneke,[30] John Berberian, Jr.,[3] Francois Bouchy,[18] Brendan P. Bowler,[31] César Briceño,[32] Christopher J. Burke,[21] Matthew R. Burleigh,[26] Sarah L. Casewell,[26] David Ciardi,[33] Kevin I. Collins,[3] Benjamin F. Cooke,[1,2] Olivier D. S. Demangeon,[9,10] Rodrigo F. Díaz,[34] C. Dorn,[19] Diana Dragomir,[35] Courtney Dressing,[36] Xavier Dumusque,[18] Néstor Espinoza,[37] P. Figueira,[38] Benjamin Fulton,[39] E. Furlan,[33] E. Gaidos,[40] C. Geneser,[41] Samuel Gill,[1] Michael R. Goad,[26] Erica J. Gonzales,[42,43] Varoujan Gorjian,[44] Maximilian N. Günther,[21] Ravit Helled,[19] Beth A. Henderson,[26] Thomas Henning,[45] Aleisha Hogan,[26] Saeed Hojjatpanah,[9,10] Jonathan Horner,[6] Andrew W. Howard,[46] Sergio Hoyer,[47] Dan Huber,[48] Howard Isaacson,[6,49] James S. Jenkins,[50,51] Eric L. N. Jensen,[52] Andrés Jordán,[4,5] Stephen R. Kane,[53] Richard C. Kidwell, Jr., John Kielkopf,[54] Nicholas Law,[55] Monika Lendl,[18] M. Lund,[56] Rachel A. Matson,[57] Andrew W. Mann,[55] James McCormac,[1,2] Matthew W. Mengel,[6] Farisa Y. Morales,[44] Louise D. Nielsen,[18] Jack Okumura,[6] Hugh P. Osborn,[21,56] Erik A. Petigura,[58] Peter Plavchan,[3] Don Pollacco,[1,2] Elisa V. Quintana,[29] Liam Raynard,[26] Paul Robertson,[59] Mark E. Rose,[16] Arpita Roy,[60] Michael Reefe,[3] Alexandre Santerne,[50] Nuno C. Santos,[9,10] Paula Sarkis,[45] J. Schlieder,[29] Richard P. Schwarz,[61] Nicholas J. Scott,[16] Avi Shporer,[21] A. M. S. Smith,[62] C. Stibbard,[3] Chris Stockdale,[63] Paul A. Strøm,[1,2] Joseph D. Twicken,[16] Thiam-Guan Tan,[64] A. Tanner,[41] J. Teske,[65,66,67] Rosanna H. Tilbrook,[26] C. G. Tinney,[68] Stephane Udry,[18] Jesus Noel Villaseñor,[21] Jose I. Vines,[69] Sharon X. Wang,[67] Lauren M. Weiss,[48] Richard G. West,[1,2] Peter J. Wheatley,[1,2] Duncan J. Wright,[6] Hui Zhang[70] and F. Zohrabi[41]

Affiliations are listed at the end of the paper

Accepted 2021 August 3. Received 2021 July 26; in original form 2020 September 30

ABSTRACT

We present the bright ($V_{mag} = 9.12$), multiplanet system TOI-431, characterized with photometry and radial velocities (RVs). We estimate the stellar rotation period to be 30.5 ± 0.7 d using archival photometry and RVs. Transiting Exoplanet Survey Satellite (*TESS*) objects of Interest (TOI)-431 b is a super-Earth with a period of 0.49 d, a radius of 1.28 ± 0.04 $R_\oplus$, a mass of 3.07 ± 0.35 $M_\oplus$, and a density of 8.0 ± 1.0 g cm^{-3}; TOI-431 d is a sub-Neptune with a period of 12.46 d, a radius of 3.29 ± 0.09 $R_\oplus$, a mass of $9.90^{+1.53}_{-1.49}$ $M_\oplus$, and a density of 1.36 ± 0.25 g cm^{-3}. We find a third planet, TOI-431 c, in the High Accuracy Radial velocity Planet Searcher RV data, but it is not seen to transit in the *TESS* light curves. It has an $M\sin i$ of $2.83^{+0.41}_{-0.34}$ $M_\oplus$, and a period of 4.85 d. TOI-431 d likely has an extended atmosphere and is one of the most well-suited *TESS* discoveries for atmospheric characterization, while the super-Earth TOI-431 b may be a stripped core. These planets straddle

★ E-mail: e.osborn@warwick.ac.uk

© 2021 The Author(s).
Published by Oxford University Press on behalf of Royal Astronomical Society. This is an Open Access article distributed under the terms of the Creative Commons Attribution License (http://creativecommons.org/licenses/by/4.0/), which permits unrestricted reuse, distribution, and reproduction in any medium, provided the original work is properly cited.

Downloaded from https://academic.oup.com/mnras/article/507/2/2782/6348103 by guest on 16 August 2022

the radius gap, presenting an interesting case-study for atmospheric evolution, and TOI-431 b is a prime *TESS* discovery for the study of rocky planet phase curves.

Key words: planets and satellites: detection – planets and satellites: fundamental parameters – planets and satellites: individual: (TOI-431, TIC 31374837).

1 INTRODUCTION

The discoveries of the *Kepler* Space Telescope (Borucki et al. 2010) provided us with the means to make statistical studies on the exoplanet population for the first time: *Kepler* has shown us that Neptune-sized planets are more common than large gas giants (Fressin et al. 2013), and that super-Earths are the most abundant planet type (Petigura, Howard & Marcy 2013). It became possible to look for trends that might elucidate planetary formation mechanisms; one such trend discovered is a bi-modality in the radius distribution of small planets. Often dubbed the 'photoevaporation valley,' the commonly posited explanation for its existence is photoevaporation of close-in planetary atmospheres (Owen & Wu 2017; Fulton et al. 2017; Fulton & Petigura 2018; Van Eylen et al. 2018; Cloutier & Menou 2020). Planets above the radius gap have retained gaseous envelopes, while planets below are theorized to have been stripped of any gas to become naked cores. Multiplanet systems have been discovered containing planets that lie both below and above the radius gap (e.g. Günther et al. 2019; Cloutier et al. 2020a), and such systems are important when considering how evolution mechanisms may sculpt the radius gap as they allow testing of atmospheric evaporation and bulk composition models.

Further to the discovery of the radius gap, a paucity of intermediate-sized planets at short periods ($\leq$3 d) dubbed the 'Neptune/sub-Jovian Desert' (Szabó & Kiss 2011; Beaugé & Nesvorný 2013; Helled, Lozovsky & Zucker 2016; Lundkvist et al. 2016; Mazeh, Holczer & Faigler 2016; Owen & Lai 2018), can be seen in both the mass-period and radius-period distribution of exoplanets, and Mazeh et al. (2016) and Owen & Lai (2018) derived boundaries for this triangular-shaped region, and the potential mechanisms behind their existence.

The Transiting Exoplanet Survey Satellite (*TESS*, Ricker et al. 2015) is now building upon the legacy of *Kepler*. Unlike *Kepler*, *TESS* has been optimized to look at bright stars, enabling high precision radial velocity (RV) follow up of planetary candidates to determine their masses, and additional follow up (with the James Webb Space Telescope, JWST, for example) will allow us to study their atmospheres. Over the course of its 2 yr primary mission, which came to an end in July 2020, over 2000 *TESS* Objects of Interest (TOIs) were released, and there have been many discoveries that contribute to fulfilling its Level-1 mission goal to measure the masses and radii of at least 50 planets with radii smaller than 4 $R_\oplus$ (e.g. Huang et al. 2018; Gandolfi et al. 2018; Cloutier et al. 2019; Dragomir et al. 2019; Dumusque et al. 2019; Luque et al. 2019; Díaz et al. 2020; Armstrong et al. 2020; Astudillo-Defru et al. 2020; Cloutier et al. 2020a,b; Nielsen et al. 2020).

We present here the discovery of TOI-431 b, c, and d. TOI-431 b and d are a super-Earth and sub-Neptune, respectively, discovered first by *TESS* and confirmed via extensive follow up: high-precision Doppler spectroscopy from the High Accuracy Radial velocity Planet Searcher (HARPS; Pepe et al. 2002) and the HIgh REsolution Spectrograph (HIRES; Vogt et al. 1994), which allows us to determine their masses; additional Doppler spectroscopy from iSHELL (Rayner et al. 2016a), Fiberfed Extended Range Optical Spectrograph (FEROS; Kaufer & Pasquini 1998), and MINERVA-Australis (Addison et al. 2019a); ground-based transit detections from Next Generation Transit Survey (NGTS; Wheatley et al. 2018) and the LCOGT 1m network (Brown et al. 2013); and a double-transit from the Spitzer space telescope. Both TOI-431 b and d contribute to the *TESS* Level-1 mission goal. TOI-431 c is an additional planet that we have found in the HARPS RV data, and it is not seen to transit. We describe the observations made and the stellar analysis of the TOI-431 system in Section 2; our joint-fit model of the system in Section 3; and put this system into context in Section 4.

2 OBSERVATIONS

2.1 Photometry

2.1.1 TESS photometry

The TOI-431 system (TIC 31374837, HIP 26013) was observed in *TESS* Sectors 5 (November 15–December 11 2018) and 6 (2018 December 15–2019 January 6) on Camera 2 in the 2-min cadence mode ($t_{\rm exp}$ = 2 min). TOI-431.01 (now TOI-431 d) was flagged on 2019 February 8 by the MIT Quick-Look Pipeline (Huang et al. 2019) with a signal-to-noise ratio (SNR) of 58; the Sector 5 light curve reveals two deep transits of TOI-431 d, but further transits of this planet fell in the data gaps in S6. TOI-431 d passed all Data Validation tests (see Twicken et al. 2018) and model fitting (see Li et al. 2019); additionally, the difference image centroiding results place the transit signature source within ~3 arcsec of the target star. TOI-431.02 (now TOI-431 b) was flagged later, on June 6, after identification by the TESS Science Processing Operations Center (SPOC) pipeline (Jenkins et al. 2016) with an SNR of 24 in a combined transit search of Sectors 5–6.

We used the publicly available photometry provided by the SPOC pipeline, and used the Presearch Data Conditioning Simple Aperture Photometry (PDCSAP_FLUX), which has common trends and artefacts removed by the SPOC Presearch Data Conditioning (PDC) algorithm (Twicken et al. 2010; Smith et al. 2012; Stumpe et al. 2012, 2014). The median-normalized PDCSAP flux, without any further detrending, is shown in the top panel of Fig. 1.

2.1.2 LCOGT photometry

To confirm the transit timing and depth, and to rule out a nearby eclipsing binary (NEB) as the source of the *TESS* transit events, we obtained three seeing-limited transit observations of TOI-431 d in the *zs*-band. The light curves were obtained using the 1-m telescopes at the Cerro Tololo Inter-American Observatory (CTIO) and the Siding Springs Observatory (SSO) as part of the Las Cumbres Observatory Global Telescope network (LCOGT; Brown et al. 2013). Both telescopes are equipped with a 4096 × 4096 Sinistro camera with a fine pixel scale of 0.39 arcsec pixel^{-1}.

We calibrated each sequence of images using the standard LCOGT BANZAI pipeline (McCully et al. 2018). The observations were scheduled using the *TESS* Transit Finder, a customized version of the TAPIR software package (Jensen 2013). The differential light curves of TOI-431, and seven neighboring sources within 2.5 arcmin based on the Gaia DR2 (Gaia Collaboration et al. 2018), were derived from uncontaminated apertures using ASTROIMAGEJ (AIJ; Collins et al.

Downloaded from https://academic.oup.com/mnras/article/507/2/2782/6348103 by guest on 16 August 2022

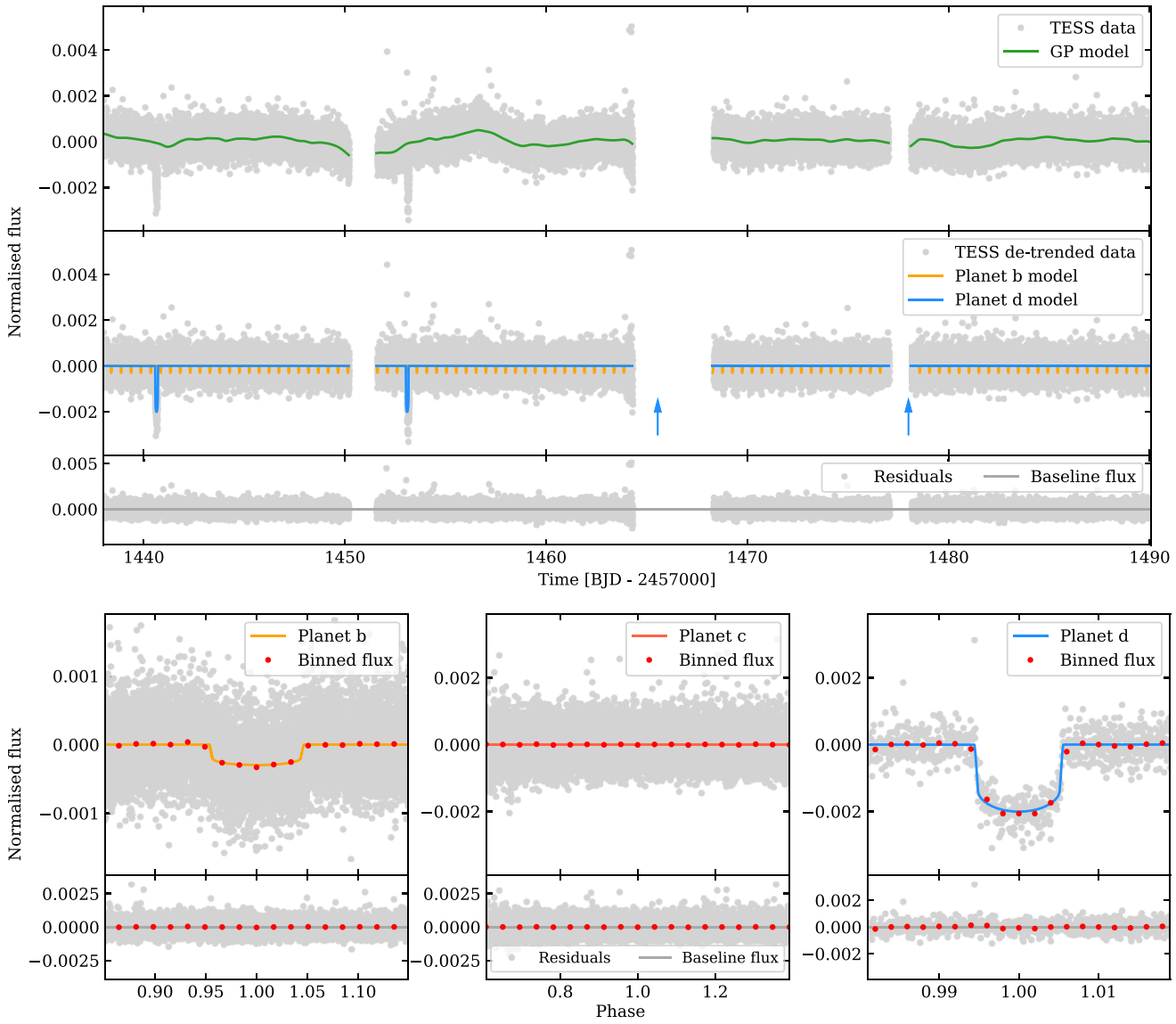


Figure 1. The *TESS* data for TOI-431 in Sectors 5 and 6. Top plot: detrending the *TESS* light curves and fitting models for TOI-431 b and c. Top: the full, 2-min cadence PDCSAP light curve, with no detrending for stellar activity, is shown in grey. Each sector has two segments of continuous viewing, and the gaps in the data correspond to the spacecraft down-linking the data to Earth after a *TESS* orbit of 13.7 d. Overlaid in green is the GP model that has been fit to this data (described in Section 3.2.1), in order to detrend the stellar activity. Middle: the flux detrended with the GP model, with the transit models for TOI-431 b (orange) and d (blue) overlaid. The expected transit times for the two further transits of TOI-431 d, both of which fall in the data down-link, are marked with blue arrows. Bottom: residuals when the best-fitting model and GP have been subtracted from the PDCSAP flux. The baseline flux (normalized to 0) is shown in dark grey. Bottom plot: phase folds of the *TESS* data for TOI-431 b (left), c (middle, with no transit evident), and d (right), with the flux binned as red circles, and the residuals of the folds once the best-fitting models have been subtracted from the flux shown in the bottom panels.

2017). Two partial transits were obtained on UT 2019 December 9, which covered the ingress and egress events from CTIO and SSO, respectively (Fig. 2). We then obtained a second ingress observation on 2020 January 3 from CTIO. Within each light curve, we detected the partial transit event on-target and cleared the field of NEBs down to $\Delta zs = 6.88$ mag.

2.1.3 *PEST photometry*

We also obtained a seeing-limited observation during the time of transit of TOI-431 d on UT 2020 February 13 using the *Perth Exoplanet Survey Telescope (PEST)* near Perth, Australia. The 0.3-m telescope is equipped with a 1530 × 1020 SBIG ST-8XME camera with an image scale of 1.″2 pixel^{-1}, resulting in a 31 × 21 arcmin^2 field of view. A custom pipeline based on C-MUNIPACK[1] was used to calibrate the images and extract the differential photometry, using an aperture with radius 6.″2. The images have typical stellar point spread functions with a full width at half-maximum (FWHM) of ∼5 arcsec. Because the transit depth of TOI-431 d is too shallow to detect from the ground with PEST, the target star was intentionally saturated to check the fainter nearby stars for possible NEBs that

[1] http://c-munipack.sourceforge.net

Downloaded from https://academic.oup.com/mnras/article/507/2/2782/6348103 by guest on 16 August 2022

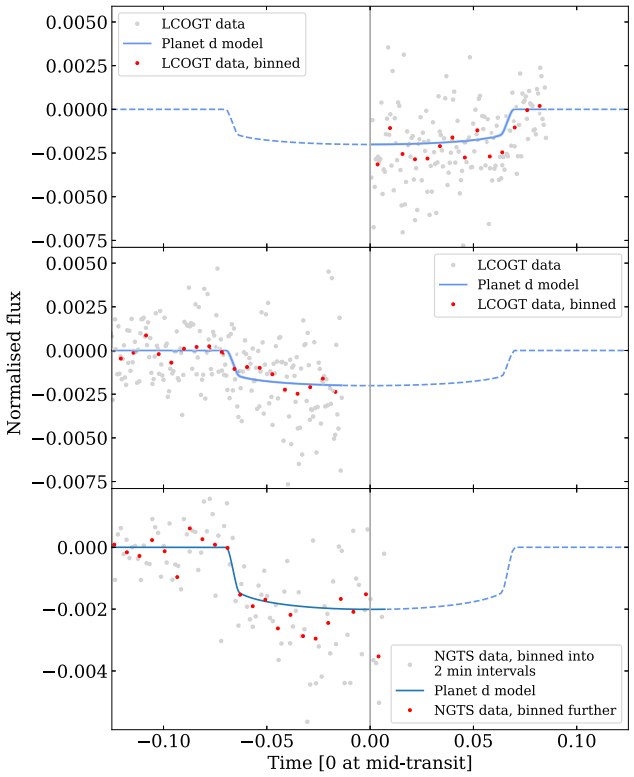


Figure 2. Best-fitting models of TOI-431 d to the LCOGT ingress (top), egress (middle), and NGTS light curves (bottom). In the LCOGT panels (top and middle), the observed flux is shown as light grey circles, the binned flux as red circles. In the NGTS panel (bottom), the flux is binned to 2-min intervals in light grey. In all panels, the fit model is given as the blue line, solid where there are photometry points, and dashed where there are not.

could be blended in the *TESS* aperture. The data rule out NEBs in all 17 stars within 2.′5 of the target star that are bright enough (*TESS* magnitude <17.4) to cause the *TESS* detection of TOI-431 d.

2.1.4 *Spitzer photometry*

Shortly after TOI-431 was identified and announced as a *TESS* planet candidate, we identified TOI-431 d as an especially interesting target for atmospheric characterization via transmission spectroscopy. We therefore scheduled one transit observation with the Spitzer Space Telescope to further refine the transit ephemeris and allow efficient scheduling of future planetary transits. We observed the system as part of Spitzer GO 14084 (Crossfield et al. 2018) using the 4.5 μm channel of the IRAC instrument (Fazio et al. 2004). We observed in subarray mode, which acquired 985 sets of 64 subarray frames, each with 0.4 s integration time. These transit observations spanned UT times from 2019 May 23 21:13 to 2019 May 24 04:42, and were preceded and followed by shorter integrations observed off-target to check for bad or hot pixels. Our transit observations used Spitzer/IRAC in PCRS Peak-up mode to place the star as closely as possible to the well-characterized 'sweet spot' on the IRAC2 detector.

2.1.5 *NGTS photometry*

The NGTS (Wheatley et al. 2018) is an exoplanet hunting facility which consists of twelve 20-cm diameter robotic telescopes and is situated at ESO's Paranal Observatory. Each NGTS telescope has a wide field of view of eight square degrees and a plate scale of 5 arcsec pixel^{-1}. NGTS observations are also afforded sub-pixel level guiding through the DONUTS auto-guiding algorithm (McCormac et al. 2013). A transit event of TOI-431 d was observed using five NGTS telescopes on 2020 February 20. On this night, a total of 5922 images were taken across the five telescopes, with each telescope observing with the custom NGTS filter and an exposure time of 10 s. The dominant photometric noise sources in NGTS light curves of bright stars are Gaussian and uncorrelated between the individual telescope systems (Bryant et al. 2020; Smith et al. 2020). As such, we can use simultaneous observations with multiple NGTS telescopes to obtain high precision light curves.

All the NGTS data for TOI-431 were reduced using a custom aperture photometry pipeline, which uses the SEP library for both source extraction and photometry (Bertin & Arnouts 1996; Barbary 2016). Bias, dark, and flat-field image corrections are found to not improve the photometric precision achieved, and so we do not apply these corrections during the image reduction. SEP and GAIA (Gaia Collaboration 2016, 2018) are both used to identify and rank comparison stars in terms of their brightness, colour, and CCD position relative to TOI-431 (for more details on the photometry, see Bryant et al. 2020).

2.2 Spectroscopy

2.2.1 *HARPS high-resolution spectroscopy*

TOI-431 was observed between 2019 February 2 and October 21 with the HARPS spectrograph mounted on the ESO 3.6-m telescope at the La Silla Observatory in Chile (Pepe et al. 2002). A total of 124 spectra were obtained under the NCORES large programme (ID 1102.C-0249, PI: Armstrong). The instrument (with resolving power $R = 115\,000$) was used in high-accuracy mode, with an exposure time of 900 s. Between 1 and 3 observations of the star were made per night. The standard offline HARPS data reduction pipeline was used to reduce the data, and a K5 template was used in a weighted cross-correlation function (CCF) to determine the radial velocities (RVs). Each epoch has further calculation of the bisector span (BIS), FWHM, and contrast of the CCF. This data are presented in Table C1.

In addition to this, there are 50 publicly available archival HARPS spectra dating from 2004 to 2015.

2.2.2 *HIRES high-resolution spectroscopy*

We obtained 28 high-resolution spectra of TOI-431 on the High Resolution Echelle Spectrometer of the 10-m Keck I telescope (Keck/HIRES; Vogt et al. 1994). The observation spans a temporal baseline from 2019 November 11 to 2020 September 27. We obtained an iodine-free spectrum on 2019 November 8 as the template for RV extraction. All other spectra were obtained with the iodine cell in the light path for wavelength calibration and line profile modeling. Each of these spectra were exposed for 4–8 min achieving a median SNR of 200 per reduced pixel near 5500 Å. The spectra were analysed with the forward-modeling Doppler pipeline described in Howard et al. (2010) for RV extraction. We analysed the Ca II H & K lines and extracted the $S_{\rm HK}$ using the method of Isaacson & Fischer (2010). These data are presented in Table C2.

2.2.3 *iSHELL spectroscopy*

We obtained 108 spectra of TOI-431 during 11 nights with the iSHELL spectrometer on the *NASA Infrared Telescope Facility*

Downloaded from https://academic.oup.com/mnras/article/507/2/2782/6348103 by guest on 16 August 2022

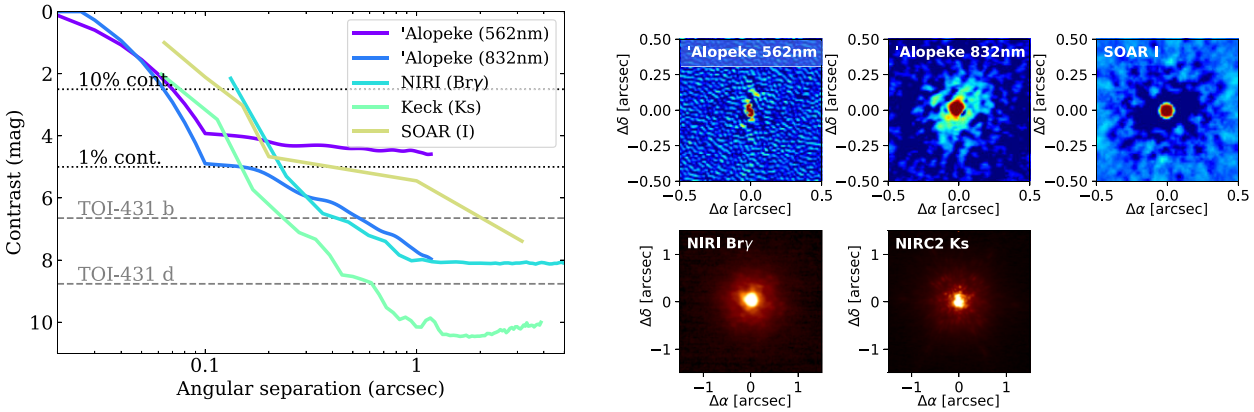


Figure 3. Left: 5σ contrast curves for all of the sources of high-resolution imaging described in Section 2.3. The 10 and 1 per cent contamination limits are given as the black dotted lines. The grey dashed lines labeled TOI-431 b and d represent the maximum contrast magnitude that a blended source could have in order to mimic the planetary transit depth if it were an eclipsing binary. Right: a compilation of reconstructed images from 'Alopeke and SOAR and AO images from NIRI and NIRC2, with the instrument and filter labelled. No additional companions are seen.

(Rayner et al. 2016b), spanning 108 d from 2019 September to December. The exposure times were 5 min, repeated 3–14 times within a night to reach a cumulative photon SNR per spectral pixel varying from 131 to 334 at ∼2.4 μm (the approximate center of the blaze for the middle order). This achieves a per-night RV precision of 3–8 ms^{-1} with a median of 5 ms^{-1}. Spectra were reduced and RVs extracted using the methods outlined in Cale et al. (2019).

2.2.4 *FEROS spectroscopy*

TOI-431 was monitored with the FEROS (Kaufer et al. 1999), installed on the MPG2.2 m telescope at La Silla Observatory, Chile. These observations were obtained in the context of the Warm gIaNts with tEss collaboration, which focuses on the systematic characterization of *TESS* transiting warm giant planets (e.g. Brahm et al. 2019; Jordán et al. 2020). FEROS has a spectral resolution of R ≈ 48 000 and uses a comparison fibre that can be pointed to the background sky or illuminated by a Thorium-Argon lamp simultaneously with the execution of the science exposure. We obtained 10 spectra of TOI-431 between 2020 February 28 and March 12. We used the simultaneous calibration technique to trace instrumental RV variations, and adopted an exposure time of 300 s, which translated in spectra with a typical SNR per resolution element of 170. FEROS data was processed with the CERES pipeline (Brahm, Jordán & Espinoza 2017), which delivers precision RV and line BIS measurements through the cross-correlation technique. The cross-correlation was executed with a binary mask reassembling the properties of a G2-type dwarf star.

2.2.5 *MINERVA-Australis spectroscopy*

MINERVA-Australis is an array of four PlaneWave CDK700 telescopes located in Queensland, Australia, fully dedicated to the precise radial-velocity follow up of *TESS* candidates. The four telescopes can be simultaneously fiber-fed to a single KiwiSpec R4-100 high-resolution (R = 80 000) spectrograph (Barnes et al. 2012; Addison et al. 2019b, 2020). TOI-431 was observed by MINERVA-Australis in its early operations, with a single telescope, for 16 epochs between 2019 February 12 and April 17. Each epoch consists of two 30-min exposures, and the resulting radial velocities are binned to a single point. Radial velocities for the observations are derived for each telescope by cross-correlation, where the template being matched is the mean spectrum of each telescope. The instrumental variations are corrected by using simultaneous Thorium-Argon arc lamp observations.

2.3 High resolution imaging

High angular resolution imaging is needed to search for nearby sources that can contaminate the *TESS* photometry, resulting in an underestimated planetary radius, or that can be the source of astrophysical false positives, such as background eclipsing binaries. The contrast curves from all of the sources of high resolution imaging described below are displayed in Fig. 3.

2.3.1 *SOAR HRCam*

We searched for stellar companions to TOI-431 with speckle imaging with the 4.1-m Southern Astrophysical Research (SOAR) telescope (Tokovinin 2018) on UT 2019 March 17, observing in the Cousins I-band, a similar visible bandpass to *TESS*. More details of the observation are available in Ziegler et al. (2020). The 5σ detection sensitivity and speckle auto-correlation functions from the observations are shown in Fig. 3. No nearby stars were detected within 3 arcsec of TOI-431 in the SOAR observations.

2.3.2 *Gemini NIRI*

We collected high resolution adaptive optics (AOs) observations using the Gemini/NIRI instrument (Hodapp et al. 2003) on UT 2019 March 18. We collected nine images in the Brγ filter, with exposure time 0.6 s per image. We dithered the telescope by 2 arcsec between each exposure, allowing for a sky background to be constructed from the science frames themselves. We corrected individual frames for bad pixels, subtracted the sky background, and flat-corrected frames, and then co-added the stack of images with the stellar position aligned. To calculate the sensitivity of these observations, we inject fake companions and measure their S/N, and scale the brightness of these fake companions until they are recovered at 5σ. This is repeated at a number of locations in the image. We average our sensitivity over position angle, and show the sensitivity as a function of radius in Fig. 3. Our observations are sensitive to companions 4.6 mag fainter than the host at 0.2 arcsec, and 8.1 mag

Downloaded from https://academic.oup.com/mnras/article/507/2/2782/6348103 by guest on 16 August 2022

fainter than the host in the background limited regime, at separations greater than 1 arcsec.

2.3.3 *Gemini 'Alopeke*

TOI-431 was observed on UT Oct 15 2019 using the 'Alopeke speckle instrument on Gemini-North.[2] 'Alopeke provides simultaneous speckle imaging in two bands, 562 and 832 nm, with output data products including a reconstructed image, and robust limits on companion detections (Howell et al. 2011). Fig. 3 shows our results in both 562 and 832 nm filters. Fig. 3 (right) shows the 832 nm reconstructed speckle image from which we find that TOI-431 is a single star with no companion brighter than within 5–8 magnitudes of TOI-431 detected within 1.2 arcsec. The inner working angle of the 'Alopeke observations are 17 mas at 562 nm and 28 mas at 832 nm.

2.3.4 *Keck NIRC2*

As part of our standard process for validating transiting exoplanets to assess the possible contamination of bound or unbound companions on the derived planetary radii (Ciardi et al. 2015), we observed TOI-431 with infrared high-resolution AO imaging at Keck Observatory. The Keck Observatory observations were made with the NIRC2 instrument on Keck-II behind the natural guide star AO system. The observations were made on UT 2019 March 25 in the standard three-point dither pattern that is used with NIRC2 to avoid the left lower quadrant of the detector, which is typically noisier than the other three quadrants. The dither pattern step size was 3 arcsec and was performed three times.

The observations were made in the *Ks* filter ($\lambda_o = 2.196$; $\Delta\lambda = 0.336\,\mu$m) with an integration time of 1 s 20 co-adds per frame for a total of 300 s on target. The camera was in the narrow-angle mode with a full field of view of ∼10 arcsec and a pixel scale of 0.099 442 arcsec per pixel. The Keck AO observations revealed no additional stellar companions detected to within a resolution ∼0.05 arcsec FWHM (Fig. 3).

The sensitivities of the final combined AO image were determined by injecting simulated sources azimuthally around the primary target every 45° at separations of integer multiples of the central source's FWHM (Furlan et al. 2017). The brightness of each injected source was scaled until standard aperture photometry detected it with 5σ significance. The resulting brightness of the injected sources relative to the target set the contrast limits at that injection location. The final 5σ limit at each separation was determined from the average of all of the determined limits at that separation and the uncertainty on the limit was set by the rms dispersion of the azimuthal slices at a given radial distance. The sensitivity curve is shown in Fig. 3 (left), along with an image centered on the primary target showing no other companion stars (right).

2.3.5 *Unbound Blended Source Confidence (BSC) analysis*

We finally analyse all contrast light curves available for this target to estimate the probability of contamination from unbound blended sources in the *TESS* aperture that are undetectable from the available high-resolution images. This probability is called the Blended Source Confidence (BSC), and the steps for estimating it are fully described in Lillo-Box, Barrado & Bouy (2014). We use a PYTHON implementation of this approach (BSC by J. Lillo-Box) which uses the TRILEGAL[3] galactic model (v1.6 Girardi et al. 2012) to retrieve a simulated source population of the region around the corresponding target.[4] This is used to compute the density of stars around the target position (radius $r = 1°$), and to derive the probability of chance alignment at a given contrast magnitude and separation. We used the default parameters for the bulge, halo, thin/thick discs, and the lognormal initial mass function from Chabrier (2001).

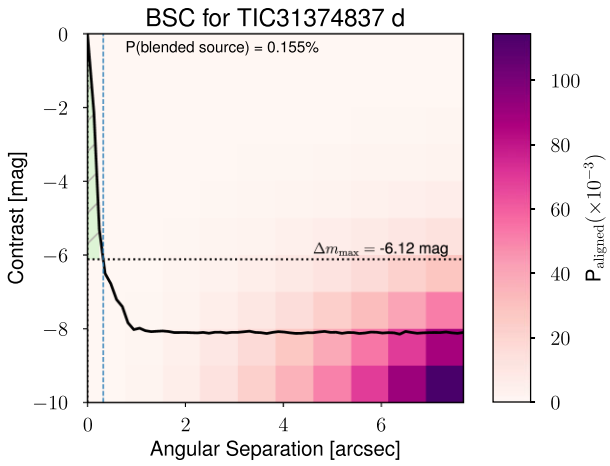


Figure 4. Contrast curve of TOI-431 from the Keck/NIRC2 instrument for the Ks filter (solid black line). The colour ($P_{\rm aligned}$) on each angular separation and contrast bin represents the probability of a chance-aligned source with these properties at the location of the target, based on TRILEGAL model (see Section 2.3.5 within the main text). The maximum contrast of a blended binary capable of mimicking the planet transit depth is shown as a dotted horizontal line. The hatched green region between the contrast curve and the maximum contrast of a blended binary (Δm_{max} line) represents the non-explored regime by the high-spatial resolution image. P(blended source) is the BSC, and this corresponds to the integration of $P_{\rm aligned}$ over the shaded region.

The contrast curves of the high-spatial resolution images are used to constrain this parameter space and estimate the final probability of undetected potentially contaminating sources. We consider as potentially contaminating sources those with a maximum contrast magnitude corresponding to $\Delta m_{\rm max} = -2.5 \log \delta$, with δ being the transit depth of the candidate planet in the *TESS* band. This offset from the target star magnitude gives the maximum magnitude that a blended star can have to mimic this transit depth. We convert the depth in the *TESS* passband to each filter (namely 562 and 832 nm for the Gemini/'Alopeke images and Ks for the rest) by using simple conversions using the TIC catalog magnitudes and linking the 562 nm filter to the SDSSr band, the 832 nm filter to the SDSSz band, and the Ks band to the 2MASS Ks filter. The corresponding conversions imply $\Delta m_{562\,\rm nm} = 0.954 \Delta m_{\rm TESS}$, $\Delta m_{832\,\rm nm} = 0.920 \Delta m_{\rm TESS}$, and $\Delta m_{\rm Ks} = 0.919 \Delta m_{\rm TESS}$. In Fig. 4, we show an example of the BSC calculation for the Keck/NIRC2 image that illustrates the method.

We applied this technique to TOI-431. The transits of the two planets in this system could be mimicked by blended eclipsing binaries with magnitude contrasts up to $\Delta m_{\rm b,max} = 6.65$ mag and $\Delta m_{\rm d,max} = 8.76$ mag in the *TESS* passband. This analysis is then especially relevant for the smallest planet in the system as the

[2] https://www.gemini.edu/sciops/instruments/alopeke-zorro/

[3] http://stev.oapd.inaf.it/cgi-bin/trilegal

[4] This is done in Python by using the Bhatti et al. (2020) implementation.

Downloaded from https://academic.oup.com/mnras/article/507/2/2782/6348103 by guest on 16 August 2022

probability of a chance-aligned star increases rapidly with fainter magnitudes. However, the high quality of the high-spatial resolution images provide a very low probability for an undetected source capable of mimicking the transit signal. For TOI-431 b, we find 0.034 per cent ('Alopeke/562 nm), 0.019 per cent ('Alopeke/832 nm), 0.13 per cent (Keck/NIRC2/Ks), and 0.54 per cent (Gemini-North/NIRI/Ks). For TOI-431 d, we find 0.009 per cent ('Alopeke/562 nm), 0.002 per cent ('Alopeke/832 nm), 0.04 per cent (Keck/NIRC2/Ks), and 0.16 per cent (Gemini-North/NIRI/Ks).

2.4 Stellar analysis

The parameters of the host star are required in order to derive precise values for the planetary ages, as well as the masses and radii, leading to bulk densities. This requires a good spectrum with high enough signal to noise and high spectral resolution. Our RV spectra fulfil these requirements after co-adding the 124 individual HARPS spectra, resulting in a spectrum with a signal to noise of about 380 per pixel at 5950 Å. We perform two independent spectroscopic analysis methods to derive the host star parameters, and further spectral energy distribution (SED) fitting.

2.4.1 Method 1: equivalent widths with ARES+MOOG:

The stellar atmospheric parameters ($T_{\rm eff}$, log g, microturbulence, and [Fe/H]) and respective error bars were derived using the methodology described in Sousa (2014); Santos et al. (2013). In brief, we make use of the equivalent widths (EW) of iron lines, as measured in the combined HARPS spectrum of TOI-431 using the ARES v2 code[5] (Sousa et al. 2015), and we assume ionization and excitation equilibrium. The process makes use of a grid of Kurucz model atmospheres (Kurucz 1993) and the radiative transfer code MOOG (Sneden 1973). This analysis results in values of effective temperature $T_{\rm eff} = 4740 \pm 94$ K, surface gravity log $g = 4.20 \pm 0.27$, microturbulence $V_{\rm tur} = 0.62 \pm 0.28$, and metallicity [Fe/H] $= 0.06 \pm 0.04$ dex. The value for log g can be corrected according to Mortier et al. (2014), to give 4.46 ± 0.27 (corrected for asteroseismology log g values) and 4.63 ± 0.28 (corrected for transit log g values). Stellar abundances of the elements were derived using the classical curve-of-growth analysis method assuming local thermodynamic equilibrium (e.g. Adibekyan et al. 2012, 2015; Delgado Mena et al. 2017). For the abundance determinations, we used the same tools and models as for stellar parameter determination. Unfortunately, due to the low $T_{\rm eff}$ of this star, we could not determine reliable abundances of carbon and oxygen. The derived abundances are presented in Table 2 and they are normal for a star with a metallicity close to solar.

In addition, we derived an estimated age by using the ratios of certain elements (the so-called chemical clocks) and the formulas presented in Delgado Mena et al. (2019). Since this star has a close to solar metallicity and is very cool (and thus probably outside the applicability limits of formulas using stellar parameters in addition to the chemical clock), we chose to use the 1D formulas presented in table 5 of Delgado Mena et al. (2019). Due to the high error in Sr abundances, we derived ages only from the abundance ratios [Y/Mg], [Y/Zn], [Y/Ti], [Y/Si], [Mg/Fe], [Ti/Fe], [Si/Fe], and [Zn/Fe]. The abundance errors of cool stars are quite large and in turn the individual age errors of each chemical clock are also large ($\gtrsim$3 Gyr) but the dispersion among them is smaller. We obtained a weighted average age of 5.1 ± 0.6 Gyr which is significantly older than the age obtained in Section 2.4.3. Nevertheless, we note that ages for very cool stars obtained from chemical clocks are affected by large errors and must be taken with caution.

[5]The last version of ARES code (ARES v2) can be downloaded at http://www.astro.up.pt/~sousasag/ares.

2.4.2 Method 2: synthesis of the entire optical spectrum

We also derived stellar properties by analysing parts of the optical spectrum in a different way by comparing the normalized, co-added spectrum with modeled synthetic spectra obtained with the Spectroscopy Made Easy (SME) package (Valenti & Piskunov 1996; Piskunov & Valenti 2017) version 5.22, with atomic parameters from the VALD database (Piskunov et al. 1995). The 1D, plane-parallel LTE synthetic spectra are calculated using stellar parameters obtained from either photometry or a visual inspection of the spectrum as a starting point. The synthetic spectrum is automatically then compared to a grid of stellar atmospheric models. The grid we used in this case is based on the MARCS models (Gustafsson et al. 2008). An iterative χ^2 minimization procedure is followed until no improvement is achieved. We refer to recent papers, e.g. Persson et al. (2018) and Gustafsson et al. (2008) for details about the method. In order to limit the number of free parameters we used empirical calibrations for the $V_{\rm mic}$ and $v_{\rm mac}$ turbulence velocities (Bruntt et al. 2010; Doyle et al. 2014). The value of $T_{\rm eff}$ was determined from fitting the Balmer Hα line wings. We used the derived $T_{\rm eff}$ to fit a large sample of [Fe I], Mg I and Ca I lines, all with well established atomic parameters in order to derive the abundance, [Fe/H], the rotation, and the surface gravity, log g. We found the star to be slowly rotating, with $v \sin i_\star = 2.5 \pm 0.6$ km s^{-1}. The star is cool, and the effective temperature as derived from the Hα line wings is $T_{\rm eff} = 4846 \pm 73$ K. Using this value for $T_{\rm eff}$ we found the [Fe/H] to be 0.20 ± 0.05 and the surface gravity log g to be 4.60 ± 0.06 (Table 2).

In order to check our result, we also analysed the same co-added spectrum using the public software package SPECMATCH-EMP (Yee, Petigura & von Braun 2017). This program extracts part of the spectrum and attempts to match it to a library of about 400 well characterized spectra of all types. Our input spectrum has to conform to the format of SPECMATCH-EMP, and we refer to Hirano et al. (2018) to describe our procedure for doing this. We derive a $T_{\rm eff}$ of 4776 ± 110 K, an iron abundance of [Fe/H] $= 0.15 \pm 0.09$ dex, and a stellar radius of $R_\star = 0.76 \pm 0.18$ R$_\odot$. The former two values are in good agreement with the results from the SME analysis.

Because of the higher precision in the SME analysis, the final adopted value of $T_{\rm eff}$ for TOI-431 is 4850 ± 75 K. Note that the error here is the internal errors in the synthesis of the spectra and does not include the inherent errors of the model grid itself, as well as those errors caused by using 1D models.

The results from this method are in agreement with those found in Section 2.4.1, with $T_{\rm eff}$ and [Fe/H] (using SPECMATCH-EMP) agreeing within error. The value for log$g$ also agrees with the corrected log$g$ values from the previous method. We therefore adopt the results from this method to take forward.

2.4.3 SED fitting

As an independent check on the derived stellar parameters, and in order to determine an estimate for stellar age, we performed an analysis of the broadband SED. Together with the *Gaia* EDR3 parallax, we determine an empirical measurement of the stellar radius following the procedures described in Stassun & Torres (2016), Stassun, Collins & Gaudi (2017), and Stassun et al. (2018). We

Downloaded from https://academic.oup.com/mnras/article/507/2/2782/6348103 by guest on 16 August 2022

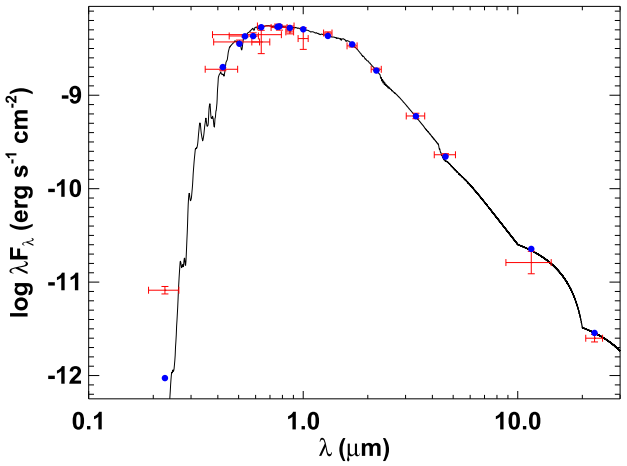


Figure 5. SED of TOI-431. Red symbols represent the observed photometric measurements, where the horizontal bars represent the effective width of the passband. Blue symbols are the model fluxes from the best-fitting Kurucz atmosphere model (black).

Table 1. Details of the TOI-431 system.

Property	Value	Source
Identifiers		
TIC ID	31374837	TICv8
HIP ID	26013	
2MASS ID	05330459-2643286	2MASS
Gaia ID	2908664557091200768	GAIA EDR3
Astrometric properties		
RA (J2016.0)	$05^h33^m04^s.62$	GAIA EDR3
Dec. (J2016.0)	$-26°43'25''.86$	GAIA EDR3
Parallax (mas)	30.65 ± 0.01	GAIA EDR3
Distance (pc)	32.61 ± 0.01	Bailer-Jones et al. (2021)
μ_{RA} (mas yr^{-1})	16.89 ± 0.01	GAIA EDR3
$\mu_{Dec.}$ (mas yr^{-1})	150.78 ± 0.01	GAIA EDR3
Photometric properties		
TESS (mag)	8.171 ± 0.006	TICv8
B (mag)	10.10 ± 0.03	TICv8
V (mag)	9.12 ± 0.03	TICv8
G (mag)	8.7987 ± 0.0003	GAIA EDR3
J (mag)	7.31 ± 0.03	2MASS
H (mag)	6.85 ± 0.03	2MASS
K (mag)	6.72 ± 0.02	2MASS

Sources: TICv8 (Stassun et al. 2019), 2MASS (Skrutskie et al. 2006), and Gaia Early Data Release 3 (Gaia Collaboration 2021)

pulled the $B_T V_T$ magnitudes from *Tycho-2*, the *grizy* magnitudes from Pan-STARRS, the JHK_S magnitudes from *2MASS*, the W1–W4 magnitudes from *WISE*, and the $GG_{RP}G_{BP}$ magnitudes from *Gaia*. Together, the available photometry spans the full stellar SED over the wavelength range 0.35–22 μm (see Fig. 5). In addition, we pulled the near UV (NUV) flux from *GALEX* in order to assess the level of chromospheric activity, if any.

We performed a fit using Kurucz stellar atmosphere models, with the effective temperature ($T_{\rm eff}$) and metallicity ([Fe/H]) adopted from the spectroscopic analysis (Section 2.4.2). The extinction (A_V) was set to zero because of the star being very nearby (Table 1). The resulting fit is excellent (Fig. 5) with a reduced χ^2 of 3.3 (excluding the *GALEX* NUV flux, which is consistent with a modest level of chromospheric activity; see below). Integrating the (unreddened) model SED gives

Table 2. Stellar parameters for TOI-431. Section references describing the method used to find the parameters are given in the table footer.

Parameter (unit)	Value	Ref
Effective temperature $T_{\rm eff}$ (K)	4850 ± 75	1
Surface gravity log g (cgs)	4.60 ± 0.06	1
Microturbulence $V_{\rm tur,mic}$ (km s^{-1})	0.8 ± 0.1 (fixed)	1
Macroscopic turbulence $V_{\rm tur,mac}$ (km s^{-1})	0.5 ± 0.1 (fixed)	1
Bolometric flux F_{bol} (10^{-9} erg s^{-1} cm^{-2})	7.98 ± 0.19	2
Stellar radius R$_*$ (R$_\odot$)	0.731 ± 0.022	2
Stellar mass M$_*$ (M$_\odot$)	0.78 ± 0.07	2
Rotation period $P_{\rm rot}$ (days)	30.5 ± 0.7	3
$v \sin i_\star$	2.5 ± 0.6	1
Chemical Abundances (dex)	**Value**	**Ref**
Metallicity [Fe/H]	0.2 ± 0.05	1
[NaI/H]	0.22 ± 0.14	4
[MgI/H]	0.10 ± 0.07	4
[AlI/H]	0.21 ± 0.10	4
[SiI/H]	0.11 ± 0.13	4
[CaI/H]	0.06 ± 0.15	4
[TiI/H]	0.17 ± 0.17	4
[CrI/H]	0.12 ± 0.11	4
[NiI/H]	0.14 ± 0.08	4

1: Section 2.4.2
2: Section 2.4.3
3: From WASP-South, see Section 2.5
4: Section 2.4.1

the bolometric flux at Earth of $F_{\rm bol} = 7.98 \pm 0.19 \times 10^{-9}$ erg s^{-1} cm^{-2}. Taking the $F_{\rm bol}$ and $T_{\rm eff}$ together with the *Gaia* EDR3 parallax, with no systematic offset applied (see e.g. Stassun & Torres 2021), gives the stellar radius as $R = 0.731 \pm 0.022$ R$_\odot$. Finally, estimating the stellar mass from the empirical relations of Torres, Andersen & Giménez (2010) and a 6 per cent error from the empirical relation itself gives $M = 0.77 \pm 0.05$ M$_\odot$, whereas the mass estimated empirically from the stellar radius together with the spectroscopic log g gives $M = 0.78 \pm 0.07$ M$_\odot$.

We can also estimate the stellar age by taking advantage of the observed chromospheric activity together with empirical age-activity-rotation relations. For example, taking the chromospheric activity indicator $\log R'_{HK} = -4.69 \pm 0.05$ from the archival HARPS data and applying the empirical relations of Mamajek & Hillenbrand (2008) gives a predicted age of 1.9 ± 0.3 Gyr. Finally, we can further corroborate the activity-based age estimate by also using empirical relations to predict the stellar rotation period from the activity. For example, the empirical relation between R'_{HK} and rotation period from Mamajek & Hillenbrand (2008) predicts a rotation period for this star of 29.8 ± 3.7 d, which is compatible with the rotation period inferred from the WASP-South observations (see Section 2.5). All of the stellar parameter values derived in this section can also be found in Table 2.

2.5 Stellar activity monitoring

Two instruments were used during different time periods to monitor TOI-431 in order to investigate the rotation period of the star. This is important to disentangle the effect of stellar activity when fitting for any planets present in the system.

WASP-South, located in Sutherland, South Africa, was the southern station of the WASP transit survey (Pollacco et al. 2006). The data reported here were obtained while WASP-South was operating as an array of 85 mm, f/1.2 lenses backed by 2048×2048 CCDs, giving a plate scale of 32 arcsec/pixel. The observations spanned 180 d in

Downloaded from https://academic.oup.com/mnras/article/507/2/2782/6348103 by guest on 16 August 2022

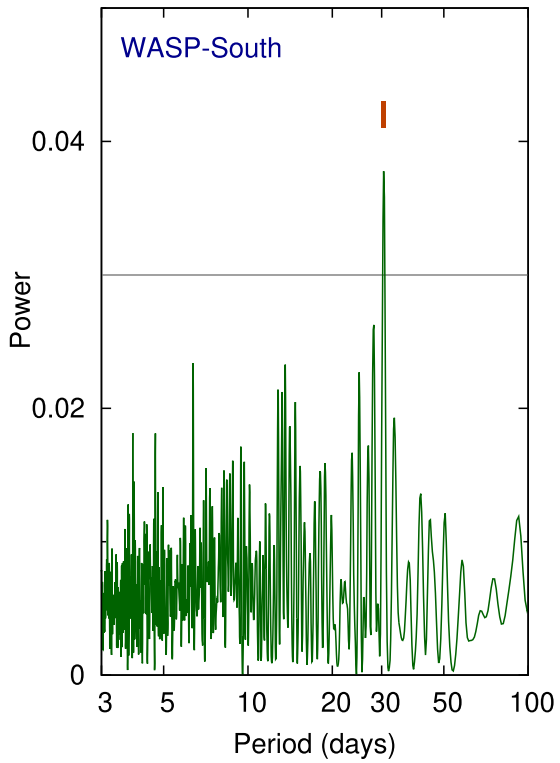


Figure 6. The periodogram of the WASP-South data for TOI-431 from 2012 to 2014. The orange tick is at 30.5 d, while the horizontal line is at the estimated 1 per cent false-alarm probability.

2012, 175 d in 2013, and 130 d in 2014. Observations on clear nights, with a typical 10-min cadence, accumulated 52 800 photometric data points.

We searched the data sets for rotational modulations, both separately and by combining the 3 yr, using the methods described by Maxted et al. (2011). We detect a persistent modulation with an amplitude of 3 mmag and a period of 30.5 ± 0.7 d (where the error makes allowance for phase shifts caused by changing starspot patterns). The periodogram from the combined 2012–2014 data are shown in Fig. 6. The modulation is significant at the 99.9 per cent level (estimated using methods from Maxted et al. 2011). In principle, it could be caused by any star in the 112 arcsec photometric extraction aperture, but all the other stars are more than 4 mag fainter.

Given the near-30-d time-scale, we need to consider the possibility of contamination by moonlight. To check this, we made identical analyses of the light curves of five other stars of similar brightness nearby in the same field. None of these show the 30.5 d periodicity.

A single NGTS telescope was used to monitor TOI-431 between the dates of 2019 October 11 and 2020 January 20. During this time period, a total of 79 011 images were taken with an exposure time of 10 s using the custom NGTS filter (520–890 nm). These data show a significant periodicity at 15.5 d, at approximately half the period of the WASP-South modulation.

As the WASP-South period agrees with the activity signal we see in the HARPS data (see Fig. 7), we therefore take the 30.5 d period value forward.

3 THE JOINT FIT

3.1 The third planet found in the HARPS data

We initially ran a joint fit which included only the planets flagged by the *TESS* pipelines, i.e. TOI-431 b and d. We then removed the signals of these planets from the raw HARPS radial velocities, and examined the residuals. This led to the discovery of an independent sinusoidal signal being seen as a significant peak in a periodogram of the residuals. This is shown in Fig. 7: from the periodogram of the raw RV data produced on DACE,[6] signals from TOI-431 b and d can be seen at 0.491 and 12.57 d, respectively, with false-alarm probabilities (FAP) of <0.1 per cent. A large signal can also be seen at 29.06 d; this is near the rotation period of the star found with WASP-South (see Section 2.5). Removing the fit for these two planets and the stellar activity reveals another signal at 4.85 d which does not correlate with any of the activity indicators (FWHM, BIS, S-Index, and H α-Index; see Fig. B1 for periodograms of these indicators for both the current and archival HARPS data), and which is not an alias of the other planetary signals.

Phase folding the *TESS* photometry on the RV period reveals no transit (see Fig. 1, bottom plot, middle panel). We also attempted to use Transit Least Squares (Hippke & Heller 2019) to recover this planet; it did not return any evidence of a transit at or near the RV period. As this planet is not evident in the *TESS* data, but is large enough to be detectable (see Section 3.3), we therefore make the assumption that it does not transit. As such, we conclude that this is a further, apparently non-transiting planet, and include it in the final joint-fit model (described in Section 3.2) when fitting the RV data.

3.2 Construction of the joint-fit model

Using the EXOPLANET package (Foreman-Mackey et al. 2020), we fit the photometry from *TESS*, LCOGT, NGTS, and *Spitzer* and the RVs from HARPS and HIRES simultaneously with Gaussian Processes (GPs) to remove the effects of stellar variability. EXOPLANET utilizes the light-curve modeling package STARRY (Luger et al. 2019), PYMC3 (Salvatier, Wiecki & Fonnesbeck 2016), and CELERITE (Foreman-Mackey et al. 2017) to incorporate GPs. While we use a GP kernel included in the EXOPLANET package for the *TESS* data, we construct our own GP kernel using PYMC3 for the HARPS and HIRES data. For consistency, all timestamps were converted to the same time system used by *TESS*, i.e. BJD - 2457000. All prior distributions set on the fit parameters of this model are given in Table A1.

3.2.1 Photometry

The flux is normalized to zero for all of the photometry by dividing the individual light curves by the median of their out-of-transit points and taking away one. To model the planetary transits, we used a limb-darkened transit model following the Kipping (2013b) quadratic limb-darkening parametrization, and Keplerian orbit models. This Keplerian orbit model is parametrized for each planet individually in terms of the stellar radius R_* in solar radii, the stellar mass M_* in solar masses, the orbital period P in days, the time of a reference transit t_0, the impact parameter b, the eccentricity e, and the argument of

[6]The DACE platform is available at https://dace.unige.ch

Downloaded from https://academic.oup.com/mnras/article/507/2/2782/6348103 by guest on 16 August 2022

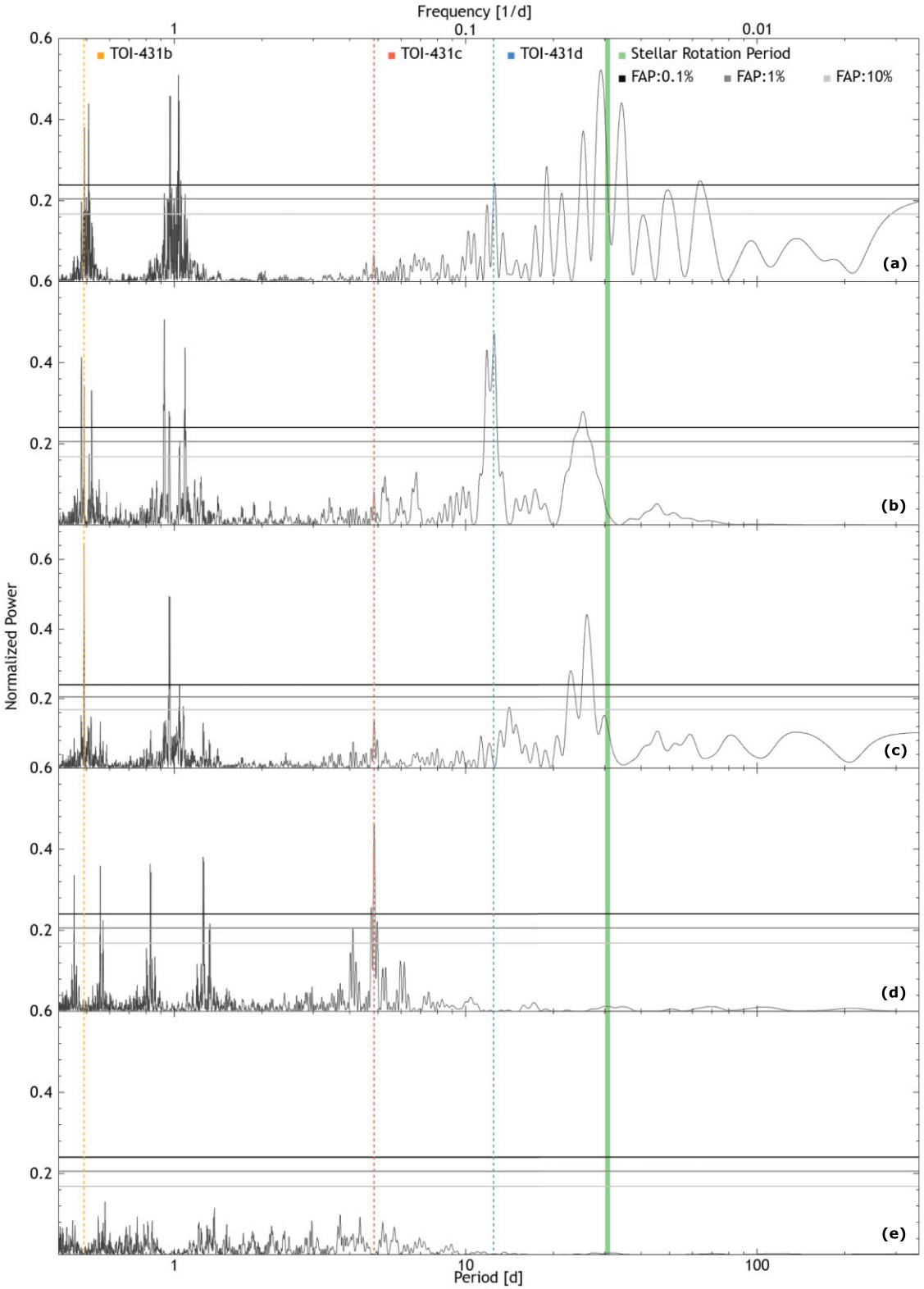


Figure 7. Periodograms for the HARPS data, where (going from top to bottom) the highest power peak has been sequentially removed until there is no power left. The best-fitting periods (see Table 3) of TOI-431 b (yellow), c (red), and d (blue), have been denoted by dotted lines, and the one standard deviation interval of the rotation period of the star has been shaded in green. The periodogram for the raw RV data is shown in panel (a); (b) has the stellar activity GP model removed; (c) has the best-fitting model for planet d also removed. Panel (d) has planet b removed, meaning that there should be no further power left. However, there is a peak evident at 4.85 d above the 0.1 per cent FAP that does not correlate with any stellar activity indicators, and it is not an alias of any other peaks. Taking this as an extra planet in the system (TOI-431 c) and removing the best-fitting model for this leaves a periodogram with no further signals, shown in panel (e).

Downloaded from https://academic.oup.com/mnras/article/507/2/2782/6348103 by guest on 16 August 2022

periastron ω. While a similar Keplerian orbit model is parametrized for the third planet, b is not defined in this case as no transit is seen in the photometric data. We find the eccentricity of all planets to be consistent with 0: when eccentricity is a fit parameter in an earlier run of this model, we find the 95 per cent confidence intervals for the eccentricity of TOI-431 b, c, and d to be 0–0.28, 0–0.22, and 0–0.31, respectively. Therefore, we fix e and ω to 0 for all planets in the final joint-fit model. These parameters are then input into light-curve models created with STARRY, together with parameters for the planetary radii R_p, the time series of the data t, and the exposure time $t_{\rm exp}$ of the instrument. As we are modeling multiple planets and multiple instruments with different $t_{\rm exp}$, a separate light-curve model is thus created per instrument for the planets that are expected to have a transit event during that data set. In some cases, TOI-431 b and d will have model light curves (e.g. in the *TESS* and *Spitzer* observations); in others (e.g. the LCOGT and NGTS observations), only TOI-431 d is expected to be transiting. TOI-431 c is not seen to transit, therefore we do not need to model it in this way. We use values from the TESS pipelines to inform our priors on the epochs, periods, transit depths, and radii of the transiting planets.

3.2.2 TESS

Both TOI-431 b and d are transiting in the *TESS* light curve, so we first create model light curves for each using STARRY.

As seen in Fig. 1, the TESS Sector 5 and 6 light curves show some stellar variability. This variability was thus modeled with the SHOTerm GP given in EXOPLANET,[7] which represents a stochastically driven, damped harmonic oscillator. We set this up using the hyperparameters $\log(S_0)$, $\log(S_w4)$, $\log(\omega_0)$, and Q. The prior on Q was set to $1/\sqrt{2}$. Priors on $\log(S_0)$ and $\log(S_w4)$ were set as normal distributions with a mean equal to the log of the variance of the flux and a standard deviation of 0.1. The prior on $\log(\omega_0)$ was also set as a normal distribution but with a mean of 0 and a standard deviation of 0.1 (see Table A1).

We then take the sum of our model light curves and subtract these from the total PDCSAP flux, and this resultant transit-free light curve is the data that the GP is trained on to remove the stellar variability. The GP model can be seen in Fig. 1 (top plot, top panel), and the resultant best-fitting model in the middle panel. Further to this, phase folds of the *TESS* data for all planets in the system can also be seen in Fig. 1 (bottom plot), where TOI-431 c has been folded on its period determined from the RV data, and no dip indicative of a transit can be seen.

3.2.3 LCOGT

No further detrending to that outlined in Section 2.1.2 was included for the LCOGT data. Only TOI-431 d is transiting in this data, so we create a model light curve of TOI-431 d using STARRY (as outlined above) per LCOGT data set to produce two model light curves overall, as there are two transit events – an ingress and an egress – on separate nights. For each data set, we use a normal prior with the model light curve as the mean and a standard deviation set to the error on the LCOGT data points, and this is then compared to the observed light curve. The best-fitting model for both the ingress and egress data is shown in Fig. 2 (top 2 panels).

[7] ⟨?PMU?⟩https://docs.exoplanet.codes/en/stable/user/api/#exoplanet.gp.terms.SHOTerm

3.2.4 NGTS

No further detrending was needed for the NGTS data after the pipeline reduction outlined in Section 2.1.5, and again, only TOI-431 d is evident in these data. Thus the same simple method used for the LCOGT data above is also applied here, creating a singular model light curve of TOI-431 d for the NGTS data and comparing this to the observed light curve, with a standard deviation set to the error on the NGTS data points. The best-fitting model for the NGTS data is shown in Fig. 2 (bottom panel).

3.2.5 Spitzer and Pixel Level Decorrelation

For the *Spitzer* double-transit observation, model light curves are created for both TOI-431 b and d. *Spitzer* data are given as N pixel values on a grid; in this instance, the grid is 3×3 pixels as in Fig. 3 of Deming et al. (2015). We follow the Pixel Level Decorrelation (PLD) method of Deming et al. (2015; summarized below) to remove the systematic effect caused by intra-pixel sensitivity variations. Together with pointing jitter, these variations mask the eclipses of exoplanets in the photometry with intensity fluctuations that must be removed. We outline our PLD implementation as follows:

First, the intensity of pixel i at each time step t, i.e. P_i^t, is normalized such that the sum of the nine pixels at one-time step is unity, thus removing any astrophysical variations:

$$\hat{P}_i^t = \frac{P_i^t}{\sum_{i=1}^{N} P_i^t}. \quad (1)$$

PLD makes the simplification that the total flux observed can be expressed as a linear equation:

$$\Delta S^t = \sum_i^N c_i \hat{P}_i^t + DE(t) + ft + gt^2 + h, \quad (2)$$

where ΔS^t is the total fluctuation from all sources. The normalized pixel intensities are multiplied by some coefficient c_i, and summed with the eclipse model $DE(t)$, a quadratic function of time $ft + gt^2$, which represents the time-dependent 'ramp', and an offset constant h. We use the eclipse model set up earlier using EXOPLANET as $DE(t)$, where D is the eclipse depth. This allows us to remove the intra-pixel effect, while solving for the eclipse amplitude and temporal baseline effects. Overall, the PLD alone has 14 free parameters that we solve for: nine pixel coefficients, the depth of eclipse and the eclipse model, two-time coefficients, and an offset term.

We add an additional fit parameter by introducing a *Spitzer* 'jitter' term. We can estimate a prior for this fit parameter by removing our best-fitting model from the total raw flux from Spitzer, and calculating the standard deviation of the residual flux, which is approximately 337 ppm.

Our overall model for the *Spitzer* data is the PLD terms multiplied by the sum of the individual light-curve models for each planet, b and d. We use a normal distribution with this model as the mean and a standard deviation set by the jitter parameter, and this is fit to the observed *Spitzer* flux. This can be seen in Fig. 8.

3.2.6 RVs

We do not include the iSHELL, FEROS, or MINERVA-Australis RVs in our joint fit, as they were not found to improve the fit due to large error bars in comparison to the HARPS and HIRES data; however, they are shown to be consistent with the result of our fit (see Fig. 9). We also do not include the archival HARPS data due to a large

Downloaded from https://academic.oup.com/mnras/article/507/2/2782/6348103 by guest on 16 August 2022

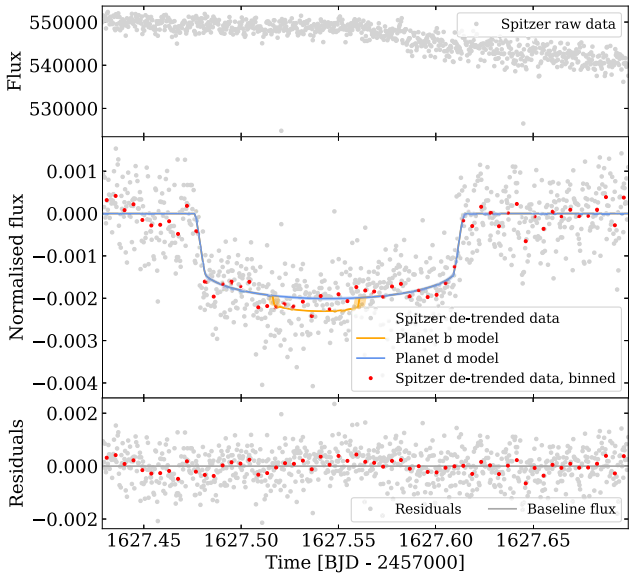


Figure 8. The *Spitzer* double-transit. Top: the raw *Spitzer* data, without any PLD applied. Middle: the *Spitzer* light curve detrended with PLD in grey and binned as red circles, with the best-fitting models of planet b (orange) and d (blue) overlaid. Bottom: the residuals when the best-fitting model has been subtracted from the detrended flux.

scatter in cadence and quality in comparison to the purpose-collected HARPS data.

3.2.7 HARPS and HIRES fitting

In this joint-fit model, we fit the HARPS and HIRES data using the same method and so they are described here in tandem. We first find predicted values of RV for each planet at each HARPS and HIRES timestamp using EXOPLANET. We set a wide uniform prior on K for each planet, the uniform distributions centered upon K values found when fitting the RV data with simple Keplerian models for all of the planets in DACE. We fit separate 'offset' terms for HARPS and HIRES to model the systematic RV, giving this a normal prior with a mean value predicted in DACE. We also fit separate 'jitter' terms, setting wide normal priors on these, the means of which are set to double the log of the minimum error on the HARPS and HIRES data, respectively.

The RV data also show significant stellar variability due to stellar rotation, and so we model this variability using another GP (see Fig. 9, top panel of top plot). This activity can be modeled as a Quasi-Periodic signal as starspots moving across the surface of the star evolve in time and are modulated by stellar rotation. In this case, we create our own Quasi-Periodic kernel using PyMC3, as no such kernel is available in EXOPLANET. PyMC3 provides a range of simple kernels[8] which are easy to combine. We use their `Periodic`:

$$k(x,x') = \eta^2 \exp\left(-\frac{\sin^2\left(\pi|x-x'|\frac{1}{T}\right)}{2l_p^2}\right), \quad (3)$$

and `ExpQuad` (squared exponential):

$$k(x,x') = \eta^2 \exp\left(-\frac{(x-x')^2}{2l_e^2}\right) \quad (4)$$

[8]https://docs.pymc.io/api/gpxs/cov.html

kernels. The hyperparameters are η (the amplitude of the GP), T (the recurrence time-scale, equivalent to the P_{rot} of the star), l_p (the smoothing parameter), and l_e (the time-scale for growth and decay of active regions; see e.g. Rasmussen & Williams 2006; Haywood et al. 2014; Grunblatt, Howard & Haywood 2015).

We multiply these kernels together to create our final Quasi-Periodic kernel:

$$k(x,x') = \eta^2 \exp\left(-\frac{\sin^2\left(\pi|x-x'|\frac{1}{T}\right)}{2l_p^2} - \frac{(x-x')^2}{2l_e^2}\right). \quad (5)$$

We use the same GP to fit the HARPS and HIRES data together using the same hyperparameters. We use a normal distribution with a mean equal to the rotation period of the star found by WASP-South (see Section 2.5 and Table 2) to set a wide prior on T.

To bring everything together, we add the predicted RVs together with the offsets, and subtract these from their respective observed RV values. This is then used as the prior on the GP, which is also given a noise term that is equal to an addition of the jitters with the squared error on the RV data.

3.3 Fit results

We first use EXOPLANET to maximize the log probability of the PyMC3 model. We then use the fit parameter values which obtains as the starting point of the PyMC3 sampler, which draws samples from the posterior using a variant of Hamiltonian Monte Carlo, the No-U-Turn Sampler. By examining the chains from earlier test runs of the model, we allow for 1000 burn-in samples which are discarded, and 5000 steps with 15 chains.

We present our best-fitting parameters for the TOI-431 system from our joint fit in Table 3. TOI-431 b is a super-Earth with a mass of $3.07^{+0.35}_{-0.34}$ $M_\oplus$ and a radius of 1.28 ± 0.04 $R_\oplus$, and from this we can infer a bulk density of $7.96^{+1.05}_{-0.99}$ g cm^{-3}. This puts TOI-431 b below the radius gap, and it is likely a stripped core with no gaseous envelope. A period of 0.49 d puts TOI-431 b in the rare ultra-short period (USP) planet category (defined simply as planets with $P <$ 1 d); examples of systems which have USP planets include Kepler-78 (Winn, Sanchis-Ojeda & Rappaport 2018), WASP-47 (Becker et al. 2015), and 55 Cancri (Dawson & Fabrycky 2010). TOI-431 c has a minimum mass of $2.83^{+0.41}_{-0.34}$ $M_\oplus$, but the lack of transits does not allow us to fit a radius. We can use the mass-radius relation via FORECASTER (Chen & Kipping 2017) to estimate a radius of $1.44^{+0.60}_{-0.34}$ $R_\oplus$, which would place this planet as another super-Earth. TOI-431 d is a sub-Neptune with a mass of $9.90^{+1.53}_{-1.49}$ $M_\oplus$ and a radius of $3.29^{+0.09}_{-0.08}$ $R_\oplus$, implying a bulk density of $1.36^{0.25}_{-0.24}$ g cm^{-3}. This lower density implies that TOI-431 d probably has a gaseous envelope. We further analyse these planets in the following section.

4 DISCUSSION

The architecture of this system is unusual in which the middle planet, TOI-431 c, is non-transiting, while the inner and outer planets are both seen to transit. Examples of this can be seen in Kepler-20 (Buchhave et al. 2016), a six-planet system where the fifth planet out from the star does not transit, but the sixth does, and HD 3167 (Vanderburg et al. 2016; Christiansen et al. 2017; Gandolfi et al. 2017), a three-planet system where the middle planet does not transit as is the case with TOI-431. Using the impact parameter b from Table 3, we calculate inclinations for TOI-431 b and d of $(84.5^{+1.1}_{-1.3})^\circ$ and $89.7 \pm 0.2^\circ$, respectively (Table 3). We can calculate a limit on the inclination for TOI-431 c assuming $b = 1$, which results in an

Downloaded from https://academic.oup.com/mnras/article/507/2/2782/6348103 by guest on 16 August 2022

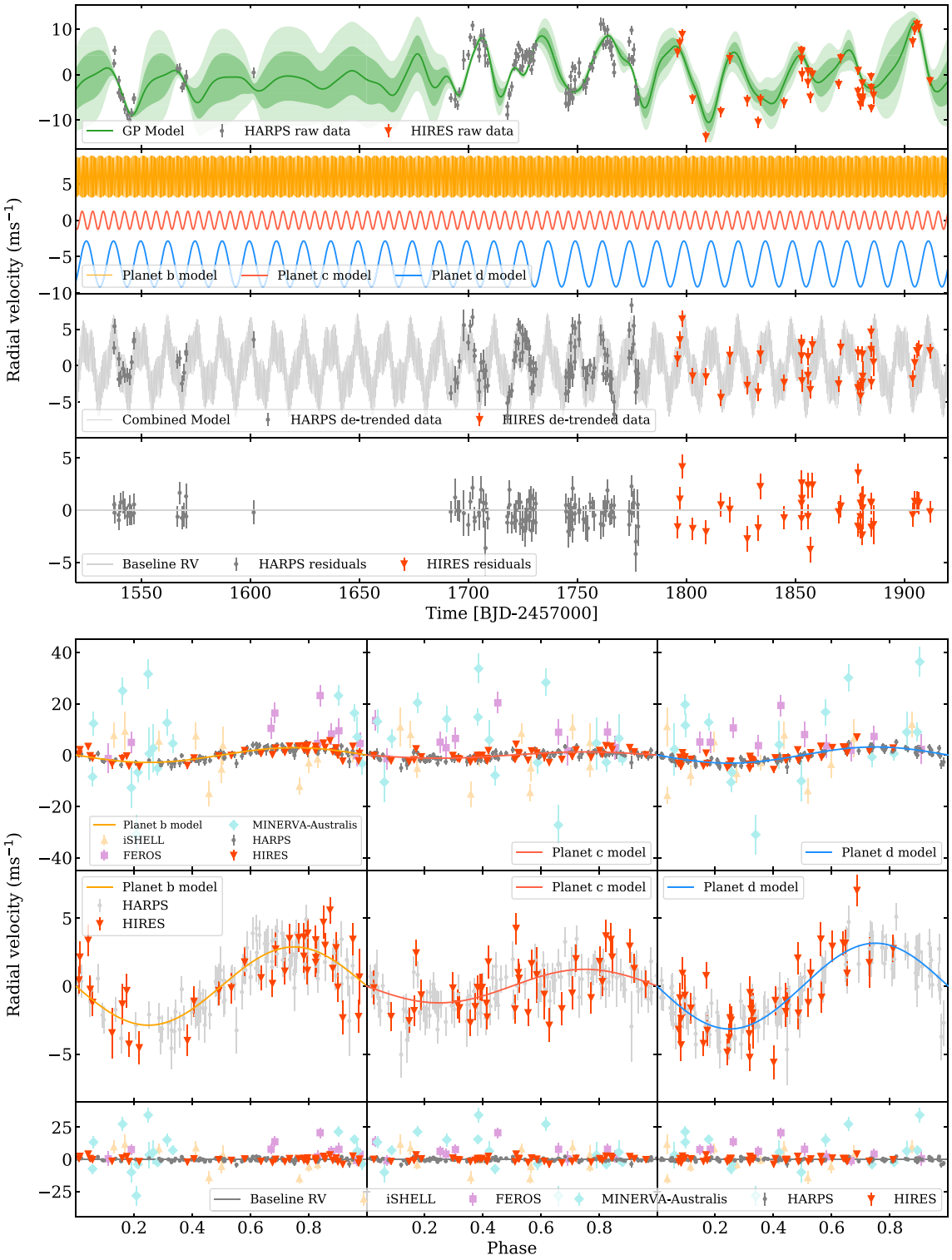


Figure 9. RV data plots, where the HARPS data are denoted as grey circles, HIRES as red upside down triangles, iSHELL as pale orange triangles, FEROS as pale pink squares, and MINERVA-Australis as pale turquoise diamonds. Top plot: the RV data, showing the GP and planet models that have been fit. Top: the best-fitting GP used to detrend the stellar activity in the HARPS data is shown as the green line. The green shaded areas represent the 1 and 2 standard deviations of the GP fit. Upper middle: the separate models for each planet, b (orange, offset by $+6\,\mathrm{m\,s^{-1}}$), c (red), and d (blue, offset by $-6\,\mathrm{m\,s^{-1}}$). Lower middle: the total model, representing the addition of the models for planets b, c, and d, is plotted in black, and over plotted is the HARPS and HIRES data. Bottom: the residuals after the total model, GP and offsets have been subtracted from the RV data. Bottom plot: the phase folds for each planet model, b (left), c (middle), and d (right), with the RV data over plotted. The top row shows all of the RV data (where the GP has been subtracted from each data set), the middle just the HARPS and HIRES data, and the bottom the residuals when the planet models have been subtracted from the RVs.

Downloaded from https://academic.oup.com/mnras/article/507/2/2782/6348103 by guest on 16 August 2022

Table 3. The parameters for the planets TOI-431 b, c, and d, calculated from our joint-fit model described fully in Section 3. The values are given as the median values of our samples, and the uncertainties are given as the 16th and 84th percentiles. The bulk densities are then calculated using the masses and radii, assuming a spherical planet of uniform density. A calculation of the radius of TOI-431 c can be found in Section 3.3, and discussion of the inclinations of the planets can be found in Section 4. The equilibrium temperature is calculated assuming an albedo of zero. Further joint-fit model parameters to those presented here can be found in Appendix A.

Parameter	TOI-431 b	TOI-431 c	TOI-431 d
Period P (days)	$0.490\,047^{+0.000\,010}_{-0.000\,007}$	$4.8494^{0.0003}_{-0.0002}$	$12.461\,03 \pm 0.000\,02$
Semimajor axis a (AU)	$0.0113^{+0.0002}_{-0.0003}$	0.052 ± 0.001	0.098 ± 0.002
Ephemeris t_0 (BJD-2457000)	$1627.538^{+0.003}_{-0.002}$	1625.9 ± 0.1	1627.5453 ± 0.0003
Radius R_p ($R_\oplus$)	1.28 ± 0.04	–	3.29 ± 0.09
Impact parameter b	$0.34^{+0.07}_{-0.06}$	–	$0.15^{+0.12}_{-0.10}$
Inclination i (degrees)	$84.3^{+1.1}_{-1.3}$	$< 86.35^{+0.04}_{-0.09}$	89.7 ± 0.2
Eccentricity e	0 (fixed)	0 (fixed)	0 (fixed)
The argument of periastron ω	0 (fixed)	0 (fixed)	0 (fixed)
Radial velocity semi-amplitude K (ms^{-1})	2.88 ± 0.30	$1.23^{+0.17}_{-0.14}$	3.16 ± 0.46
Mass M_p ($M_\oplus$)	3.07 ± 0.35	$2.83^{+0.41}_{-0.34}$ ($M \sin i$)	$9.90^{+1.53}_{-1.49}$
Bulk density ρ (g cm^{-3})	8.0 ± 1.0	–	1.36 ± 0.25
Equilibrium temperature T_{eq} (K)	1862 ± 42	867 ± 20	633 ± 14

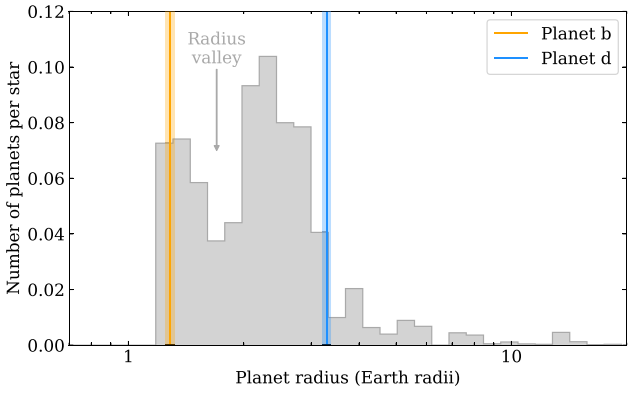


Figure 10. A histogram of planet radius for planets with orbital periods less than 100 d, as given in Fulton & Petigura (2018). The radius valley can be seen at 1.7 $R_\oplus$: below the gap are rocky super-Earths, above the gap are gaseous sub-Neptunes. TOI-431 b (orange, with 1σ confidence intervals shaded) is the former, while TOI-431 d (blue) is the latter.

inclination that must be $< (86.35^{+0.04}_{-0.09})^\circ$ in order for TOI-431 c to be non-transiting.

The TOI-431 system is a good target system for studying planetary evolution. TOI-431 b and d reside either side of the radius-period valley described in Fulton et al. (2017), Fulton & Petigura (2018), Van Eylen et al. (2018; see Fig. 10), providing a useful test-bed for the theorized mechanisms behind it. X-ray and extreme ultraviolet (EUV) driven photoevaporation is one of the two main proposed mechanisms (Owen & Wu 2017), and we investigated its effect both now and in the past in the TOI-431 system. As no direct X-ray observations of the system exist, we had to make use of empirical formulae for relating the ratio of the X-ray and bolometric luminosities to age (Jackson, Davis & Wheatley 2012) and Rossby number (related to $P_{\rm rot}$; Wright et al. 2011, 2018). We extrapolate to the EUV using the relations of King et al. (2018). Under the assumption of energy-limited escape (Watson, Donahue & Walker 1981; Erkaev et al. 2007), we estimate a current mass loss rate for TOI-431 d between 5×10^8 and 5×10^9 g s^{-1}. The same assumptions yield a current rate of 10^{10}–10^{11} g s^{-1} for TOI-431 b, but since that planet is unlikely to retain much, if any, atmosphere, the likely true rate is much lower.

Integrating the Jackson et al. (2012) relations across the lifetime of the star, and again assuming energy-limited escape, lifetime-to-date mass loss estimates of 44 per cent and 1.0 per cent for TOI-431 b and d, respectively, are found. Adding 2 per cent extra mass and doubling the radius to account for a primordial envelope around TOI-431 b raises the lifetime loss to 94 per cent. Again, the true value will be lower as XUV photoevaporation will not affect the rocky core, but rather the estimates calculated here demonstrate TOI-431 b would easily have lost a typical envelope with a mass fraction of a few per cent. The value for TOI-431 d is consistent with the density of the planet, which suggests it retains a substantial envelope.

In order to characterize the composition of TOI-431 b and d, we model the interior considering a pure-iron core, a silicate mantle, a pure-water layer, and a H-He atmosphere. The models follow the basic structure model of Dorn et al. (2017), with the equation of state (EOS) of the iron core taken from Hakim et al. (2018), the EOS of the silicate-mantle from Connolly (2009), and SCVH (Saumon, Chabrier & van Horn 1995) for the H-He envelope assuming protosolar composition. For water, we use the QEOS of Vazan et al. (2013) for low pressures and the one of Seager et al. (2007) for pressures above 44.3 GPa.

Fig. 11 shows M-R curves tracing compositions of pure-iron, Earth-like, pure-water and a planet with 95 per cent water and 5 per cent H-He atmosphere subjected to a stellar radiation of $F/F_\oplus = 50$ (comparable to the case of the TOI-431 planets), and exoplanets with accurate and reliable mass and radius determinations. It should be noted that the position of the water line in the diagram is very sensitive to used EOS (e.g. Haldemann et al. 2020). Fig. 11 shows two water lines using QEOS and EOS from Sotin, Grasset & Mocquet (2007). As shown in Fig. 11, TOI-431 b is one of the many super-Earths following the Earth-like composition line. This suggests that it is mostly made of refractory materials. TOI-431 d, instead, sits above the two the pure-water curves and below the 5 per cent curve, implying that the H-He mass fraction is unlikely to exceed a few per cent. Its density is lower than most of the observed sub-Neptunes. There are three planets in the catalogue presented in Otegi, Bouchy & Helled (2020b) with masses below 10 $M_\oplus$ and radii above 3 $R_\oplus$ (Kepler-11 d, e and Kepler-36 c), and all of

Downloaded from https://academic.oup.com/mnras/article/507/2/2782/6348103 by guest on 16 August 2022

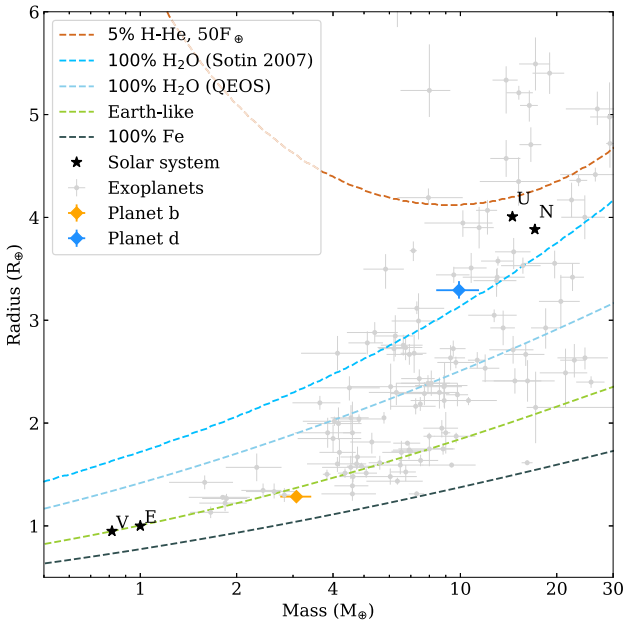


Figure 11. Mass-radius diagram of known exoplanets with mass determinations better than 4σ from the NASA exoplanet archive (https://exoplanetarchive.ipac.caltech.edu, as of 2020 September 22) shown in grey. TOI-431 b (orange) and d (blue) are denoted as diamonds, and the Solar System planets Venus (V), Earth (E), Uranus (U), and Neptune (N) are marked as black stars. Also shown are the composition lines of iron (dark grey), Earth-like (green), and pure-water planets (pale blue and mid blue, using QEOS and EOS from Sotin et al. (2007), respectively), plus an additional line representing a planet with a 95 per cent water and a 5 per cent H-He envelope with $F/F_{\oplus}$= 50, comparable to the case of the TOI-431 planets (brown).

Table 4. Inferred interior structure properties of TOI-431 b and d.

Interior Structure:	TOI-431 b	TOI-431 d
$M_{\rm core}/M_{\rm total}$	$0.51^{+0.15}_{-0.14}$	$0.29^{+0.16}_{-0.13}$
$M_{\rm mantle}/M_{\rm total}$	$0.37^{+0.27}_{-0.18}$	$0.34^{+0.23}_{-0.12}$
$M_{\rm water}/M_{\rm total}$	$0.15^{+0.12}_{-0.09}$	$0.33^{+0.21}_{-0.15}$
$M_{\rm H\text{-}He}/M_{\rm total}$	–	$0.036^{+0.012}_{-0.009}$

their masses have been determined with TTVs. As shown in Otegi et al. (2020a), reducing the uncertainties in this M-R regime would lead to significant improvements on the determination of the volatile envelope mass. As TOI-431 is in the ESPRESSO GTO target list, more observations will help to further constrain the internal structure of TOI-431 d.

We then quantify the degeneracy between the different interior parameters and produce posterior probability distributions using a generalized Bayesian inference analysis with a Nested Sampling scheme (e.g. Buchner 2014). The interior parameters that are inferred include the masses of the pure-iron core, silicate mantle, water layer and H-He atmospheres. For the analysis, we use the stellar Fe/Si and Mg/Si ratios as a proxy for the planet. Table 4 lists the inferred mass fractions of the core, mantle, water-layer, and H-He atmosphere from the interior models. It should be noted, however, that our estimates have rather large uncertainties. Indeed, in this regime of the M-R relation, there is a large degeneracy, and therefore the mass ratio between the planetary layers is not well-constrained. Nevertheless, we find that TOI-431 b has a negligible H-He envelope of $1.2\text{x}10^{-9}$ $M_{\oplus}$.

The larger companion TOI-431 d is expected to have a significant volatile layer of H-He and/or water of about 3.6 or 33 per cent of its total mass, respectively. The nature of the volatile layer is degenerate.

Considering the future observation prospects of this system, for TOI-431 d, we calculate a transmission spectroscopy metric (TSM; Kempton et al. 2018) of 215 ± 58, after propagating the uncertainties on all system parameters. The relatively large uncertainty is dominated by the uncertainty on the planet's mass; none the less, this TSM value indicates that TOI-431 d is likely among the best transmission spectroscopy targets known among small, cool exoplanets (<4 $R_{\oplus}$, <1000 K; see table 11 of Guo et al. 2020).

5 CONCLUSION

We have presented here the discovery of three new planets from the *TESS* mission in the TOI-431 system. Our analysis is based upon 2-min cadence *TESS* observations from two sectors, ground-based follow up from LCOGT and NGTS, and space-based follow up from *Spitzer*. The photometric data were modeled jointly with RV data from the HARPS spectrograph, and further RVs from iSHELL, FEROS, and MINERVA-Australis are included in our analysis. We find evidence to suggest that the host star is rotating with a period of 30.5 d, and account for this in our joint-fit model. Nearby contaminating stellar companions are ruled out by multiple sources of high resolution imaging.

TOI-431 b is a super-Earth characterized by both photometry and RVs, with an USP of 0.49 d. It likely has a negligible envelope due to substantial atmosphere evolution via photoevaporation, and an Earth-like composition.

TOI-431 c is found in the HARPS RV data and is not seen to transit. It has a period of 4.84 d and a minimum mass similar to the mass of TOI-431 b; extrapolating this minimum mass to a radius via the M-R relation places it as a likely second super-Earth.

TOI-431 d is a sub-Neptune with a period of 12.46 d, characterized by both photometry and RVs. It has likely retained a substantial H-He envelope of about 4 per cent of its total mass. Additionally, TOI-431 b and d contribute to the *TESS* Level-1 mission requirement.

This system is a candidate for further study of planetary evolution, with TOI-431 b and d either side of the radius valley. The system is bright, making it amenable to follow-up observations. TOI-431 b, in particular, would potentially be an interesting target for phase-curve observations with JWST.

ACKNOWLEDGEMENTS

This paper includes data collected by the *TESS* mission. Funding for the *TESS* mission is provided by the NASA Explorer Program. Resources supporting this work were provided by the NASA High-End Computing (HEC) Program through the NASA Advanced Supercomputing (NAS) Division at Ames Research Center for the production of the SPOC data products.

We acknowledge the use of public *TESS* Alert data from pipelines at the *TESS* Science Office and at the *TESS* Science Processing Operations Center.

This study is based on observations collected at the European Southern Observatory under ESO programme 1102.C-0249 (PI: Armstrong). Additionally, the archival HARPS data dating from 2004 to 2015 were obtained under the following programmes: 072.C-0488 (PI: Mayor); 183.C-0972 (PI: Udry); 085.C-0019 (PI: Lo Curto); 087.C-0831 (PI: Lo Curto); and 094.C-0428 (PI: Brahm).

This work was supported by grants to P.P. from NASA (award 18-2XRP18_2-0113), the National Science Foundation (Astronomy and Astrophysics grant 1716202), the Mount Cuba Astronomical

Downloaded from https://academic.oup.com/mnras/article/507/2/2782/6348103 by guest on 16 August 2022

Foundation, and George Mason University start-up funds. The NASA Infrared Telescope Facility is operated by the University of Hawaii under contract NNH14CK55B with NASA.

This paper is, in part, based on data collected under the NGTS project at the ESO La Silla Paranal Observatory. The NGTS facility is operated by the consortium institutes with support from the UK Science and Technology Facilities Council (STFC) projects ST/M001962/1 and ST/S002642/1.

This work makes use of observations from the LCOGT network.

MINERVA-Australis is supported by Australian Research Council LIEF grant LE160100001, Discovery grant DP180100972, Mount Cuba Astronomical Foundation, and institutional partners University of Southern Queensland, UNSW Sydney, MIT, Nanjing University, George Mason University, University of Louisville, University of California Riverside, University of Florida, and The University of Texas at Austin.

We respectfully acknowledge the traditional custodians of all lands throughout Australia, and recognize their continued cultural and spiritual connection to the land, waterways, cosmos, and community. We pay our deepest respects to all Elders, ancestors, and descendants of the Giabal, Jarowair, and Kambuwal nations, upon whose lands the MINERVA-Australis facility at Mt Kent is situated.

This work is based in part on observations made with the *Spitzer* Space Telescope, which was operated by the Jet Propulsion Laboratory, California Institute of Technology under a contract with NASA. Support for this work was provided by NASA through an award issued by JPL/Caltech.

Based on observations obtained at the international Gemini Observatory, a program of NSF's NOIRLab acquired through the Gemini Observatory Archive at NSF's NOIRLab, which is managed by the Association of Universities for Research in Astronomy (AURA) under a cooperative agreement with the National Science Foundation on behalf of the Gemini Observatory partnership: the National Science Foundation (United States), National Research Council (Canada), Agencia Nacional de Investigación y Desarrollo (Chile), Ministerio de Ciencia, Tecnología e Innovación (Argentina), Ministério da Ciência, Tecnologia, Inovaíes e Comunicações (Brazil), and Korea Astronomy and Space Science Institute (Republic of Korea). Data collected under program GN-2019A-LP-101.

This work was enabled by observations made from the Gemini North telescope, located within the Maunakea Science Reserve and adjacent to the summit of Maunakea. We are grateful for the privilege of observing the Universe from a place that is unique in both its astronomical quality and its cultural significance.

This work is based in part on observations obtained at the SOAR telescope, which is a joint project of the Ministério da Ciência, Tecnologia e Inovações (MCTI/LNA) do Brasil, the US National Science Foundation's NOIRLab, the University of North Carolina at Chapel Hill (UNC), and Michigan State University (MSU).

This research made use of EXOPLANET (Foreman-Mackey et al. 2020) and its dependencies (Astropy Collaboration 2013, 2018; Kipping 2013a; Agol, Luger & Foreman-Mackey 2019; Luger et al. 2019; Salvatier et al. 2016; Theano Development Team 2016; Foreman-Mackey et al. 2020).

This publication makes use of The Data & Analysis Center for Exoplanets (DACE), which is a facility based at the University of Geneva (CH) dedicated to extrasolar planets data visualization, exchange and analysis. DACE is a platform of the Swiss National Centre of Competence in Research (NCCR) PlanetS, federating the Swiss expertise in Exoplanet research. The DACE platform is available at https://dace.unige.ch.

This work has made use of data from the European Space Agency (ESA) mission *Gaia* (https://www.cosmos.esa.int/gaia), processed by the *Gaia* Data Processing and Analysis Consortium (DPAC, https://www.cosmos.esa.int/web/gaia/dpac/consortium). Funding for the DPAC has been provided by national institutions, in particular the institutions participating in the *Gaia* Multilateral Agreement.

AO is supported by an STFC studentship. DJA acknowledges support from the STFC via an Ernest Rutherford Fellowship (ST/R00384X/1). RB acknowledges support from FONDECYT Post-doctoral Fellowship Project 3180246, and from the Millennium Institute of Astrophysics (MAS). IJMC acknowledges support from the NSF through grant AST-1824644. AJ acknowledges support from FONDECYT project 1210718, and from ANID - Millennium Science Initiative - ICN12_009. MNG acknowledges support from MIT's Kavli Institute as a Juan Carlos Torres Fellow. JSJ acknowledges support by FONDECYT grant 1201371 and partial support from CONICYT project Basal AFB-170002. We acknowledge support by FCT - Fundação para a Ciência e a Tecnologia through national funds and by FEDER through COMPETE2020 - Programa Operacional Competitividade e Internacionalização by these grants: UID/FIS/04434/2019; UIDB/04434/2020; UIDP/04434/2020; PTDC/FIS-AST/32113/2017 & POCI-01-0145-FEDER-032113; PTDC/FIS-AST/28953/2017 & POCI-01-0145-FEDER-028953. VA, EDM, and SCCB acknowledge the support from FCT through Investigador FCT contracts IF/00650/2015/CP1273/CT0001, IF/00849/2015/CP1273/CT0003, and IF/01312/2014/CP1215/CT0004, respectively. ODSD is supported in the form of work contract (DL 57/2016/CP1364/CT0004) funded by FCT. CD acknowledges the SNSF Ambizione grant 174028. SH acknowledge support by the fellowships PD/BD/128119/2016 funded by FCT (Portugal). JKT acknowledges that support for this work was provided by NASA through Hubble Fellowship grant *HST*-HF2-51399.001 awarded by the Space Telescope Science Institute, which is operated by the Association of Universities for Research in Astronomy, Inc., for NASA, under contract NAS5-26555. DD acknowledges support through the TESS Guest Investigator Program grant 80NSSC19K1727. JLB and DB have been supported by the Spanish State Research Agency (AEI) Project No. MDM-2017-0737 Unidad de Excelencia 'María de Maeztu'- Centro de Astrobiología (CSIC/INTA). SH acknowledges CNES funding through the grant 837319. PJW acknowledges support from STFC through consolidated grants ST/P000495/1 and ST/T000406/1. LMW is supported by the Beatrice Watson Parrent Fellowship and NASA ADAP grant 80NSSC19K0597.

DATA AVAILABILITY

The TESS data are available from the Mikulski Archive for Space Telescopes (MAST), at https://heasarc.gsfc.nasa.gov/docs/tess/data-access.html. The other photometry from the LCOGT, NGTS, and *Spitzer* as well as all of the RV data, are available for public download from the ExoFOP-TESS archive at https://exofop.ipac.caltech.edu/tess/target.php?id=31374837. This data are labeled 'Osborn+ 2021' in their descriptions. The high-resolution imaging data are also available from the ExoFOP TESS archive. The model code underlying this article will be shared on reasonable request to the corresponding author.

REFERENCES

Addison B. et al., 2019a, PASP, 131, 115003
Addison B. et al., 2019b, PASP, 131, 115003
Addison B. C. et al., 2020, MNRAS, 502, 3704

Downloaded from https://academic.oup.com/mnras/article/507/2/2782/6348103 by guest on 16 August 2022

Adibekyan V. et al., 2015, A&A, 583, A94
Adibekyan V. Z., Sousa S. G., Santos N. C., Delgado Mena E., González Hernández J. I., Israelian G., Mayor M., Khachatryan G., 2012, A&A, 545, A32
Agol E., Luger R., Foreman-Mackey D., 2019, AJ, 159, 123
Armstrong D. J. et al., 2020, Nature, 583, 39
Astropy Collaboration, 2013, A&A, 558, A33
Astropy Collaboration, 2018, AJ, 156, 123
Astudillo-Defru N. et al., 2020, A&A, 636, A58
Bailer-Jones C. A. L., Rybizki J., Fouesneau M., Demleitner M., Andrae R., 2021, AJ, 161, 147
Barbary K., 2016, J. Open Source Softw., 1, 58
Barnes S. I., Gibson S., Nield K., Cochrane D., 2012, in Ground-based and Airborne Instrumentation for Astronomy IV, Society of Photo-Optical Instrumentation Engineers (SPIE) Conference Series. p. 844688
Beaugé C., Nesvorný D., 2013, ApJ, 763, 12
Becker J. C., Vanderburg A., Adams F. C., Rappaport S. A., Schwengeler H. M., 2015, ApJ, 812, L18
Bertin E., Arnouts S., 1996, A&AS, 117, 393
Bhatti W., Bouma L., Joshua J., Price-Whelan A., 2020, waqasbhatti/astrobase: astrobase v0.5.0
Borucki W. J. et al., 2010, Science, 327, 977
Brahm R. et al., 2019, AJ, 158, 45
Brahm R., Jordán A., Espinoza N., 2017, PASP, 129, 034002
Brown T. M. et al., 2013, PASP, 125, 1031
Bruntt H. et al., 2010, MNRAS, 405, 1907
Bryant E. M. et al., 2020, MNRAS, 494, 5872
Buchhave L. A. et al., 2016, AJ, 152, 160
Buchner J., 2014, Statistics and Computing, 26, 383
Cale B. et al., 2019, AJ, 158, 170
Chabrier G., 2001, ApJ, 554, 1274
Chen J., Kipping D., 2017, ApJ, 834, 17
Christiansen J. L. et al., 2017, AJ, 154, 122
Ciardi D. R., Beichman C. A., Horch E. P., Howell S. B., 2015, ApJ, 805, 16
Cloutier R. et al., 2019, A&A, 629, A111
Cloutier R. et al., 2020a, AJ, 160, 3
Cloutier R. et al., 2020b, AJ, 160, 22
Cloutier R., Menou K., 2020, AJ, 159, 211
Collins K. A., Kielkopf J. F., Stassun K. G., Hessman F. V., 2017, AJ, 153, 77
Connolly J. A. D., 2009, Geochem. Geophys. Geosyst., 10, Q10014
Crossfield I. et al., 2018, Spitzer Transits of New TESS Planets, Spitzer Proposal
Dawson R. I., Fabrycky D. C., 2010, ApJ, 722, 937
Delgado Mena E. et al., 2019, A&A, 624, A78
Delgado Mena E., Tsantaki M., Adibekyan V. Z., Sousa S. G., Santos N. C., González Hernández J. I., Israelian G., 2017, A&A, 606, A94
Deming D. et al., 2015, ApJ, 805, 132
Díaz M. R. et al., 2020, MNRAS, 493, 973
Dorn C., Venturini J., Khan A., Heng K., Alibert Y., Helled R., Rivoldini A., Benz W., 2017, A&A, 597, A37
Doyle A. P., Davies G. R., Smalley B., Chaplin W. J., Elsworth Y., 2014, MNRAS, 444, 3592
Dragomir D. et al., 2019, ApJ, 875, L7
Dumusque X. et al., 2019, A&A, 627, A43
Erkaev N. V., Kulikov Y. N., Lammer H., Selsis F., Langmayr D., Jaritz G. F., Biernat H. K., 2007, A&A, 472, 329
Fazio G. G. et al., 2004, ApJS, 154, 10
Foreman-Mackey D., Agol E., Ambikasaran S., Angus R., 2017, AJ, 154, 220
Foreman-Mackey D., Czekala I., Luger R., Agol E., Barentsen G., Barclay T., 2020, exoplanet-dev/exoplanet v0.2.6
Fressin F. et al., 2013, ApJ, 766, 81
Fulton B. J. et al., 2017, AJ, 154, 109
Fulton B. J., Petigura E. A., 2018, AJ, 156, 264
Furlan E. et al., 2017, AJ, 153, 71
Gaia Collaboration, 2016, A&A, 595, A2
Gaia Collaboration, 2018, A&A, 616, A1
Gaia Collaboration, 2021, A&A, 649, A1
Gandolfi D. et al., 2017, AJ, 154, 123
Gandolfi D. et al., 2018, A&A, 619, L10
Girardi L. et al., 2012, Astrophys. Space Sci. Proc., 26, 165
Grunblatt S. K., Howard A. W., Haywood R. D., 2015, ApJ, 808, 127
Günther M. N. et al., 2019, Nat. Astron., 3, 1099
Guo X. et al., 2020, AJ, 159, 239
Gustafsson B., Edvardsson B., Eriksson K., Jørgensen U. G., Nordlund Å., Plez B., 2008, A&A, 486, 951
Hakim K., Rivoldini A., Van Hoolst T., Cottenier S., Jaeken J., Chust T., Steinle-Neumann G., 2018, Icarus, 313, 61
Haldemann J., Alibert Y., Mordasini C., Benz W., 2020, A&A, 643, A105
Haywood R. D. et al., 2014, MNRAS, 443, 2517
Helled R., Lozovsky M., Zucker S., 2016, MNRAS, 455, L96
Hippke M., Heller R., 2019, Astrophysics Source Code Library, record (ascl:1910.007)
Hirano T. et al., 2018, AJ, 155, 127
Hodapp K. W. et al., 2003, PASP, 115, 1388
Howard A. W. et al., 2010, ApJ, 721, 1467
Howell S. B., Everett M. E., Sherry W., Horch E., Ciardi D. R., 2011, AJ, 142, 19
Huang C. X. et al., 2018, ApJ, 868, L39
Huang, Chelsea X., et al.,2020, Research Notes of the American Astronomical Society, 4, 204
Isaacson H., Fischer D., 2010, ApJ, 725, 875
Jackson A. P., Davis T. A., Wheatley P. J., 2012, MNRAS, 422, 2024
Jenkins J. M. et al., 2016, Society of Photo-Optical Instrumentation Engineers (SPIE) Conference Series, 9913, The TESS science processing operations center, p. 99133E
Jensen E., 2013, Astrophysics Source Code Library, record (ascl:1306.007)
Jordán A., Brahm R., Espinoza N., Henning T., Jones M. I., Kossakowski D., Sarkis P., Trifonov T., 2020, AJ, 159, 145
Kaufer A., Pasquini L., 1998, Society of Photo-Optical Instrumentation Engineers (SPIE) Conference Series, 3355, FEROS: the new fiber-linked echelle spectrograph for the ESO 1.52-m telescope, p. 844
Kaufer A., Stahl O., Tubbesing S., Nørregaard P., Avila G., Francois P., Pasquini L., Pizzella A., 1999, The Messenger, 95, 8
Kempton E. M. R. et al., 2018, PASP, 130, 114401
King G. W. et al., 2018, MNRAS, 478, 1193
Kipping D. M., 2013a, MNRAS, 435, 2152
Kipping D. M., 2013b, MNRAS, 435, 2152
Kurucz R. L., 1993, SYNTHE spectrum synthesis programs and line data
Li J., Tenenbaum P., Twicken J. D., Burke C. J., Jenkins J. M., Quintana E. V., Rowe J. F., Seader S. E., 2019, PASP, 131, 024506
Lillo-Box J., Barrado D., Bouy H., 2014, A&A, 566, A103
Luger R., Agol E., Foreman-Mackey D., Fleming D. P., Lustig-Yaeger J., Deitrick R., 2019, AJ, 157, 64
Lundkvist M. S. et al., 2016, Nat. Commun., 7, 11201
Luque R. et al., 2019, A&A, 628, A39
Mamajek E. E., Hillenbrand L. A., 2008, ApJ, 687, 1264
Maxted P. F. L. et al., 2011, PASP, 123, 547
Mazeh T., Holczer T., Faigler S., 2016, A&A, 589, A75
McCormac J., Pollacco D., Skillen I., Faedi F., Todd I., Watson C. A., 2013, PASP, 125, 548
McCully C., Volgenau N. H., Harbeck D.-R., Lister T. A., Saunders E. S., Turner M. L., Siiverd R. J., Bowman M., 2018, Society of Photo-Optical Instrumentation Engineers (SPIE) Conference Series, 10707, p. 107070K
Mortier A., Sousa S. G., Adibekyan V. Z., Brand ão I. M., Santos N. C., 2014, A&A, 572, A95
Nielsen L. D. et al., 2020, MNRAS, 492, 5399
Otegi J. F., Dorn C., Helled R., Bouchy F., Haldemann J., Alibert Y., 2020a, A&A, 640, A135
Otegi J. F., Bouchy F., Helled R., 2020b, A&A, 634, A43
Owen J. E., Lai D., 2018, MNRAS, 479, 5012
Owen J. E., Wu Y., 2017, ApJ, 847, 29
Pepe F. et al., 2002, The Messenger, 110, 9
Persson C. M. et al., 2018, A&A, 618, A33

Downloaded from https://academic.oup.com/mnras/article/507/2/2782/6348103 by guest on 16 August 2022

Petigura E. A., Howard A. W., Marcy G. W., 2013, Proc. Natl. Acad. Sci., 110, 19273
Piskunov N., Valenti J. A., 2017, A&A, 597, A16
Piskunov N. E., Kupka F., Ryabchikova T. A., Weiss W. W., Jeffery C. S., 1995, A&AS, 112, 525
Pollacco D. L. et al., 2006, PASP, 118, 1407
Rasmussen C. E., Williams C. K. I., 2006, Gaussian Processes for Machine Learning. The MIT Press
Rayner J. et al., 2016a, iSHELL: a construction, assembly and testing, 9908, Society of Photo-Optical Instrumentation Engineers (SPIE) Conference Series, p. 990884
Rayner J. et al., 2016b, in Proc. SPIE. p. 990884
Ricker G. R. et al., 2015, J. Astron. Telesc. Instrum. Syst., 1, 014003
Salvatier J., Wiecki T. V., Fonnesbeck C., 2016, PeerJ Comput. Sci., 2, e55
Santos N. C. et al., 2013, A&A, 556, A150
Saumon D., Chabrier G., van Horn H. M., 1995, ApJS, 99, 713
Seager S., Kuchner M., Hier-Majumder C. A., Militzer B., 2007, ApJ, 669, 1279
Skrutskie M. F. et al., 2006, AJ, 131, 1163
Smith J. C. et al., 2012, PASP, 124, 1000
Smith A. M. S. et al., 2020, Astron. Nachr., 341, 273
Sneden C. A., 1973, PhD thesis. Univ. Texas, Austin
Sotin C., Grasset O., Mocquet A., 2007, Icarus, 191, 337
Sousa S. G., 2014, Determination of Atmospheric Parameters of B-, A-, F- and G-Type Stars. p.297
Sousa S. G., Santos N. C., Adibekyan V., Delgado-Mena E., Israelian G., 2015, A&A, 577, A67
Stassun K. G. et al., 2019, AJ, 158, 138
Stassun K. G., Torres G., 2016, AJ, 152, 180
Stassun K. G., Torres G., 2021, ApJ, 907, L33
Stassun K. G., Collins K. A., Gaudi B. S., 2017, AJ, 153, 136
Stassun K. G., Corsaro E., Pepper J. A., Gaudi B. S., 2018, AJ, 155, 22
Stumpe M. C. et al., 2012, PASP, 124, 985
Stumpe M. C., Smith J. C., Catanzarite J. H., Van Cleve J. E., Jenkins J. M., Twicken J. D., Girouard F. R., 2014, PASP, 126, 100
Szabó G. M., Kiss L. L., 2011, ApJ, 727, L44
Theano Development Team, 2016, preprint (arXiv:1605.02688)
Tokovinin A., 2018, PASP, 130, 035002
Torres G., Andersen J., Giménez A., 2010, A&AR, 18, 67
Twicken J. D. et al., 2018, PASP, 130, 064502
Twicken J. D., Chandrasekaran H., Jenkins J. M., Gunter J. P., Girouard F., Klaus T. C., 2010, in Society of Photo-Optical Instrumentation Engineers (SPIE) Conference Series. p. 77401U
Valenti J. A., Piskunov N., 1996, A&AS, 118, 595
Van Eylen V., Agentoft C., Lundkvist M. S., Kjeldsen H., Owen J. E., Fulton B. J., Petigura E., Snellen I., 2018, MNRAS, 479, 4786
Vanderburg A. et al., 2016, ApJ, 829, L9
Vazan A., Kovetz A., Podolak M., Helled R., 2013, MNRAS, 434, 3283
Vogt S. S. et al., 1994, in Crawford D. L., Craine E. R., eds, Proc. SPIE Conf. Ser. Vol. 2198, Instrumentation in Astronomy VIII. SPIE, Bellingham, p. 362
Watson A. J., Donahue T. M., Walker J. C. G., 1981, Icarus, 48, 150
Wheatley P. J. et al., 2018, MNRAS, 475, 4476
Winn J. N., Sanchis-Ojeda R., Rappaport S., 2018, New Astron. Rev., 83, 37
Wright N. J., Drake J. J., Mamajek E. E., Henry G. W., 2011, ApJ, 743, 48
Wright N. J., Newton E. R., Williams P. K. G., Drake J. J., Yadav R. K., 2018, MNRAS, 479, 2351
Yee S. W., Petigura E. A., von Braun K., 2017, ApJ, 836, 77
Ziegler C., Tokovinin A., Briceño C., Mang J., Law N., Mann A. W., 2020, AJ, 159, 19

APPENDIX A: FURTHER JOINT-FIT PARAMETERS

Further parameters from our joint-fit model (described in Section 3) are presented in Table A1.

Table A1. Further parameters to those presented in Table 3: the prior distributions input into our joint-fit model (described fully in Section 3), and the fit values resulting from the model. The priors are created using distributions in PYMC3, and the relevant inputs to each distribution are listed. The fit values are given as the median values of our samples, and the uncertainties are given as the 16th and 84th percentiles. Where necessary, the specific planet a parameter is describing is noted in square brackets.

Parameter	Prior distribution	Fit value
Planets		
Period P [b] (days)	$\mathcal{N}(0.490\,0657, 0.001)$	$0.490\,047^{+0.000\,010}_{-0.000\,007}$
Period P [c] (days)	$\mathcal{N}(4.849\,427, 0.1)$	$4.8494^{+0.0003}_{-0.0002}$
Period P [d] (days)	$\mathcal{N}(12.461\,09, 0.01)$	$12.461\,03 \pm 0.000\,02$
Ephemeris t_0 [b] (BJD-2457000)	$\mathcal{N}(1627.533, 0.1)$	$1627.538^{+0.003}_{-0.002}$
Ephemeris t_0 [c] (BJD-2457000)	$\mathcal{N}(1625.888, 0.1)$	1625.87 ± 0.10
Ephemeris t_0 [d] (BJD-2457000)	$\mathcal{N}(1627.545, 0.1)$	1627.5453 ± 0.0003
log (R_p) [b] ($R_\odot$)	$\mathcal{N}(-4.35^*, 1.0)$	-4.44 ± 0.03
log (R_p) [d] ($R_\odot$)	$\mathcal{N}(-3.41^*, 1.0)$	-3.50 ± 0.03
Star		
Mass ($M_\odot$)	$\mathcal{N}_\mathcal{T}(0.77, 0.7, 0.0, 3.0)$	0.81 ± 0.05
Radius ($R_\odot$)	$\mathcal{N}_\mathcal{T}(0.729, 0.022, 0.0, 3.0)$	0.72 ± -0.02
TESS		
Mean	$\mathcal{N}(0.0, 1.0)$	$0.000\,06 \pm 0.000\,06$
GP log ($s2$)	$\mathcal{N}(-15.257^\dagger, 0.1)$	-15.539 ± 0.008
GP log ($w0$)	$\mathcal{N}(0.0, 0.1)$	0.19 ± 0.08
GP log ($Sw4$)	$\mathcal{N}(-15.257^\dagger, 0.1)$	-15.37 ± 0.09
LCOGT (ingress)		
Mean	$\mathcal{N}(0.0, 1.0)$	-0.00044 ± 0.00008
LCOGT (egress)		
Mean	$\mathcal{N}(0.0, 1.0)$	0.00002 ± 0.00006
NGTS		
Mean	$\mathcal{N}(0.0, 1.0)$	$-0.00015^{+0.00008}_{-0.00007}$
Spitzer		
Jitter	$\mathcal{N}(337.0, 20.0)$	345 ± 8
Pixel coefficient c_1	$\mathcal{N}(1236218, 10^5)$	$1448286^{+68271}_{-69627}$
Pixel coefficient c_2	$\mathcal{N}(468921, 10^5)$	408211^{+14963}_{-14570}
Pixel coefficient c_3	$\mathcal{N}(-917568, 10^5)$	$-832924^{+62790}_{-62527}$
Pixel coefficient c_4	$\mathcal{N}(465062, 10^5)$	428366^{+16837}_{-16824}
Pixel coefficient c_5	$\mathcal{N}(693929, 10^5)$	688664^{+10881}_{-10749}
Pixel coefficient c_6	$\mathcal{N}(554898, 10^5)$	542039^{+12467}_{-12391}
Pixel coefficient c_7	$\mathcal{N}(-205010, 10^5)$	$-194425^{+61256}_{-59207}$
Pixel coefficient c_8	$\mathcal{N}(564035, 10^5)$	522150^{+12762}_{-12784}
Pixel coefficient c_9	$\mathcal{N}(618285, 10^5)$	669652^{+22918}_{-22697}
Time dependent f ramp coefficient	$\mathcal{N}(0.0, 170000)$	2017^{+9457}_{-9651}
Time dependent g ramp coefficient	$\mathcal{N}(0.0, 170000)$	618^{+522}_{-518}
Offset constant h	$\mathcal{N}(0.0, 10^4)$	-1543^{+3755}_{-3760}
HARPS and HIRES		
HARPS Offset	$\mathcal{N}(48830.87, 10.0)$	48828 ± 2
log ($\text{Jitter}_{\text{HARPS}}$)	$\mathcal{N}(-0.2661^\ddagger, 5.0)$	$-5.06^{+2.10}_{-3.37}$
HIRES Offset	$\mathcal{N}(0.01, 10.0)$	-2.07 ± 2.34
log ($\text{Jitter}_{\text{HIRES}}$)	$\mathcal{N}(-0.2659^\ddagger, 5.0)$	$-0.05^{+0.36}_{-0.43}$
GP recurrence time-scale T (stellar rotation period) (days)	$\mathcal{N}(30.5, 0.7)$	30.7 ± 0.6

Downloaded from https://academic.oup.com/mnras/article/507/2/2782/6348103 by guest on 16 August 2022

Table A1 – *continued*

Parameter	Prior distribution	Fit value
GP amplitude η	$\mathcal{HC}(5.0)$	$5.48^{+1.12}_{-0.83}$
GP lengthscale l_e	$\mathcal{N}_{\mathcal{T}}(30.0, 20.0, 25.0, -)$	$31.5^{+6.3}_{-4.2}$
GP lengthscale l_p	$\mathcal{N}_{\mathcal{T}}(0.1, 10.0, 0.0, 1.0)$	$0.47^{+0.10}_{-0.09}$

Notes. **Distribution descriptions:** $\mathcal{N}(\mu, \sigma)$: a normal distribution with a mean μ and a standard deviation σ;
$\mathcal{N}_{\mathcal{B}}(\mu, \sigma, a, b)$: a bounded normal distribution with a mean μ, a standard deviation σ, an lower bound a, and an upper bound b (bounds optional)
$\mathcal{N}_{\mathcal{T}}(\mu, \sigma, a, b)$: a truncated normal distribution with a mean μ, a standard deviation σ, a lower bound a, and an upper bound b (bounds optional);
$\mathcal{HC}(\beta)$: a Half-Cauchy distribution with a single beta parameter β. **Prior values:**
*equivalent to $0.5(\log(D)) + \log(R_*)$ where D is the transit depth and R_* is the value of the prior on the stellar radius ($R_\odot$);
†equivalent to the log of the variance of the *TESS* flux;
‡equivalent to 2 times the log of the minimum error on the HARPS or HIRES RV data, respectively.

APPENDIX B: STELLAR ACTIVITY INDICATORS

Further to Fig. 7, periodograms of stellar activity indicators for both the archival and the purpose-collected HARPS data are presented in Fig. B1.

Downloaded from https://academic.oup.com/mnras/article/507/2/2782/6348103 by guest on 16 August 2022

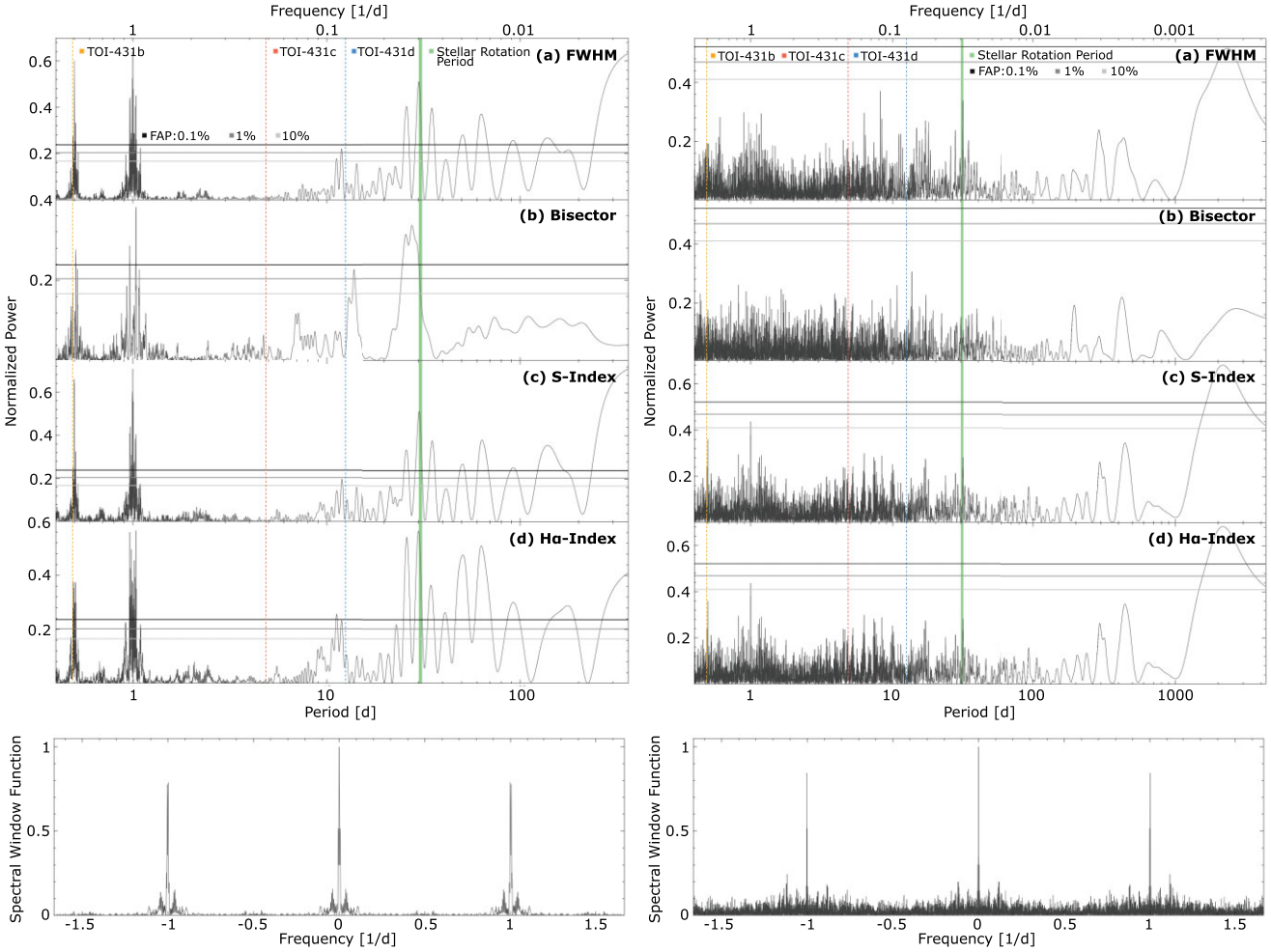


Figure B1. Periodograms for the activity indicators (top row) and window functions (bottom row) from the HARPS data, including the purpose-collected HARPS data from February to October 2019 (left), and the archival HARPS data from 2004 to 2015 (right), illustrating that there is no significant power at the 4.85 d period of TOI-431 c. The best-fitting periods (see Table 3) of TOI-431 b (yellow), c (red), and d (blue), have been denoted by dotted lines, and the 1 standard deviation interval of the rotation period of the star has been shaded in green.

APPENDIX C: DATA

The HARPS and HIRES RV data are presented in Tables C1 and C2, respectively.

Table C1. HARPS spectroscopy from February to October 2019.

Time (RJD)	RV (ms^{-1})	σ_{RV} (ms^{-1})	FWHM (ms^{-1})	Bisector (ms^{-1})	Contrast	S_{MW}
58537.53770973021	48830.979962	0.894407	6330.143967	38.148888	49.532876	0.370009
58537.655514969956	48833.848987	0.994823	6330.289387	36.923112	49.534854	0.361645
58539.53381296992	48824.538870	1.006177	6324.786911	39.072933	49.567807	0.365675
⋮	⋮	⋮	⋮	⋮	⋮	⋮

Note. The full HARPS data products can be found on ExoFOP-TESS at https://exofop.ipac.caltech.edu/tess/target.php?id=31374837

Downloaded from https://academic.oup.com/mnras/article/507/2/2782/6348103 by guest on 16 August 2022

Table C2. HIRES spectroscopy from x to x 20xx.

Time (BJD TDB)	RV (ms^{-1})	σ_{RV} (ms^{-1})
2458796.014464	4.90676701782345	1.06348240375519
2458797.0428	6.94764041206104	1.14499938488007
2458798.095775	8.81269072598892	1.1401127576828
⋮	⋮	⋮

Note. The full HIRES data products can be found on ExoFOP-TESS at https://exofop.ipac.caltech.edu/tess/target.php?id=31374837

[1]*Department of Physics, University of Warwick, Gibbet Hill Road, Coventry CV4 7AL, UK*
[2]*Centre for Exoplanets and Habitability, University of Warwick, Gibbet Hill Road, Coventry CV4 7AL, UK*
[3]*George Mason University, Physics and Astronomy Department, 4400 University Drive MS 3F3, Fairfax, VA 22030, USA*
[4]*Facultad de Ingeniería y Ciencias, Universidad Adolfo Ibáñez, Av. Diagonal las Torres 2640, Peñalolén, Santiago, Chile*
[5]*Millennium Institute for Astrophysics, Campus San Joaquín UC Facultad de Física Instituto de Astrofísica, Vicuña Mackenna, 4860, Macul, Santiago, Chile*
[6]*Centre for Astrophysics, University of Southern Queensland, West Street, Toowoomba QLD 4350 Australia*
[7]*Division of Geological and Planetary Sciences, 1200 E California Blvd, Pasadena, CA 91125, USA*
[8]*Department of Physics and Astronomy, University of Kansas, Lawrence, KS 66045, USA*
[9]*Instituto de Astrofísica e Ciências do Espaço, Universidade do Porto, CAUP, Rua das Estrelas, P-4150-762 Porto, Portugal*
[10]*Departamento de Física e Astronomia, Faculdade de Ciências, Universidade do Porto, Rua do Campo Alegre, P-4169-007 Porto, Portugal*
[11]*Center for Astrophysics | Harvard & Smithsonian, 60 Garden Street, Cambridge, MA 02138, USA*
[12]*Banting Fellow*
[13]*Leiden Observatory, Leiden University, NL-2333 CA Leiden, the Netherlands*
[14]*Department of Space, Earth and Environment, Chalmers University of Technology, Onsala Space Observatory, SE-439 92 Onsala, Sweden*
[15]*Astrophysics Group, Keele University, Staffordshire ST5 5BG, UK*
[16]*NASA Ames Research Center, Moffett Field, CA 94035, USA*
[17]*Depto. Astrofísica, Centro de Astrobiología (CSIC/INTA), ESAC Campus, E-28692 Villanueva de la Cañada (Madrid), Spain*
[18]*Observatoire de l'Université de Genève, Chemin des Maillettes 51, CH-1290 Versoix, Switzerland*
[19]*University of Zürich, Institute for Computational Science, Winterthurerstrasse 190, CH-8057 Zürich, Switzerland*
[20]*Department of Physics & Astronomy, Vanderbilt University, Nashville, TN 37235, USA*
[21]*Department of Physics and Kavli Institute for Astrophysics and Space Research, Massachusetts Institute of Technology, Cambridge, MA 02139, USA*
[22]*Dunlap Institute for Astronomy and Astrophysics, University of Toronto, 50 St. George Street, Toronto, Ontario M5S 3H4, Canada*
[23]*Department of Earth, Atmospheric and Planetary Sciences, Massachusetts Institute of Technology, Cambridge, MA 02139, USA*
[24]*Department of Aeronautics and Astronautics, MIT, 77 Massachusetts Avenue, Cambridge, MA 02139, USA*
[25]*Department of Astrophysical Sciences, Peyton Hall, 4 Ivy Lane, Princeton, NJ 08540, USA*
[26]*School of Physics and Astronomy, University of Leicester, Leicester, LE1 7RH, UK*
[27]*Department of Astronomy, University of Florida, 211 Bryant Space Science Center, Gainesville, FL 32611, USA*
[28]*University of Maryland, Baltimore County, 1000 Hilltop Circle, Baltimore, MD 21250, USA*
[29]*NASA Goddard Space Flight Center, 8800 Greenbelt Road, Greenbelt, MD 20771, USA*
[30]*Department of Physics, and Institute for Research on Exoplanets, Universite de Montreal, Montreal QC H3C 3J7, Canada*
[31]*Department of Astronomy, The University of Texas at Austin, Austin, TX 78712, USA*
[32]*Cerro Tololo Inter-American Observatory/NSF's NOIRLab, Casilla 603, La Serena 1700000, Chile*
[33]*NASA Exoplanet Science Institute, Caltech/IPAC, Mail Code 100-22, 1200 E. California Blvd., Pasadena, CA 91125, USA*
[34]*International Center for Advanced Studies (ICAS) and ICIFI (CONICET), ECyT-UNSAM, Campus Miguelete, 25 de Mayo y Francia, (1650) Buenos Aires, Argentina*
[35]*Department of Physics and Astronomy, University of New Mexico, 210 Yale Blvd NE, Albuquerque, NM 87106, USA*
[36]*Department of Astronomy, The University of California, Berkeley, CA 94720, USA*
[37]*Space Telescope Science Institute, 3700 San Martin Drive, Baltimore, MD 21218, USA*
[38]*European Southern Observatory, Alonso de Cordova 3107, Vitacura, Santiago, Chile*
[39]*NASA Exoplanet Science Institute/Caltech-IPAC, MC 314-6, 1200 E California Blvd, Pasadena, CA 91125, USA*
[40]*Department of Earth Sciences | University of Hawai'i at Mānoa, Honolulu, HI 96822, USA*
[41]*Department of Physics & Astronomy, Mississippi State University, Starkville, MS 39762, USA*
[42]*Department of Astronomy & Astrophysics, University of California, Santa Cruz, CA 95064, USA*
[43]*National Science Foundation Graduate Research Fellow*
[44]*Jet Propulsion Laboratory, California Institute of Technology, 4800 Oak Grove Drive, Pasadena, CA 91109, USA*
[45]*Max-Planck-Institut für Astronomie, Königstuhl 17, Heidelberg D-69117, Germany*
[46]*Department of Astronomy, California Institute of Technology, Pasadena, CA 91125, USA*
[47]*Aix Marseille Univ, CNRS, CNES, LAM, Marseille, 13388, France*
[48]*Institute for Astronomy, University of Hawai'i, 2680 Woodlawn Drive, Honolulu, HI 96822, USA*
[49]*501 Campbell Hall, University of California at Berkeley, Berkeley, CA 94720, USA*
[50]*Departamento de Astronomía, Universidad de Chile, Camino El Observatorio 1515, Las Condes, Santiago, Chile*
[51]*Núcleo de Astronomía, Facultad de Ingeniería y Ciencias, Universidad Diego Portales, Av. Ejército 441, Santiago, Chile*
[52]*Dept. of Physics & Astronomy, Swarthmore College, Swarthmore PA 19081, USA*
[53]*Department of Earth and Planetary Sciences, University of California, Riverside, CA 92521, USA*
[54]*Department of Physics and Astronomy, University of Louisville, Louisville, KY 40292, USA*
[55]*Department of Physics and Astronomy, The University of North Carolina at Chapel Hill, Chapel Hill, NC 27599-3255, USA*
[56]*NCCR PlanetS, Centre for Space & Habitability, University of Bern, Bern, CH-3012, Switzerland*
[57]*U.S. Naval Observatory, 3450 Massachusetts Avenue NW, Washington, D.C. 20392, USA*

Downloaded from https://academic.oup.com/mnras/article/507/2/2782/6348103 by guest on 16 August 2022

[58]*Department of Physics & Astronomy, University of California Los Angeles, Los Angeles, CA 90095, USA*
[59]*Department of Physics & Astronomy, University of California Irvine, Irvine, CA 92697, USA*
[60]*Department of Astronomy, California Institute of Technology, Pasadena, CA 91125, USA*
[61]*Patashnick Voorheesville Observatory, Voorheesville, NY 12186, USA*
[62]*Institute of Planetary Research, German Aerospace Center, Rutherford-strasse 2, D-12489 Berlin, Germany*
[63]*Hazelwood Observatory, Australia*
[64]*Perth Exoplanet Survey Telescope, Perth, Western Australia*
[65]*Earth and Planets Laboratory, Carnegie Institution for Science, 5241 Broad Branch Road NW, Washington, DC 20815, USA*
[66]*NASA Hubble Fellow*
[67]*Observatories of the Carnegie Institution for Science, 813 Santa Barbara Street, Pasadena, CA 91101, USA*
[68]*Exoplanetary Science at UNSW, School of Physics, UNSW Sydney, NSW 2052, Australia*
[69]*Departamento de Astronomía, Universidad de Chile, Casilla 36-D, Santiago, Chile*
[70]*School of Astronomy and Space Science, Key Laboratory of Modern Astronomy and Astrophysics in Ministry of Education, Nanjing University, Nanjing 210046, Jiangsu, China*

This paper has been typeset from a TEX/LATEX file prepared by the author.

Downloaded from https://academic.oup.com/mnras/article/507/2/2782/6348103 by guest on 16 August 2022